Surfaces and Interfaces xxx (xxxx) 107909

Contents lists available at ScienceDirect

Surfaces and Interfaces

journal homepage: www.elsevier.com/locate/surfin

Urea-mediated Tb-TiO_2 nanocomposites for azo dyes breakdown stimulated by UV and solar light: A smart solution for wastewater detoxification and microbial control

Sharon Leela N [a], Kannan S [a, *], T. Abisheik [b], V. Pandiyan [b], Abdullah K. Alanazi [c], A. Raja [d], Parvathalu Kalakonda [e], Arun Thirumurugan [f], Gabriela Sandoval-Hevia [g], Krishnakumar Balu [h, ij, *]

[a] Department of Physics, SRM Institute of Science and Technology, Vadapalani Campus, No.1 Jawaharlal Nehru Road, Vadapalani, Chennai 600026, Tamil Nadu, India
[b] Department of Physics, Nehru Memorial College (Autonomous), Affiliated to Bharathidasan University, Puthanampatti, Tiruchirappalli 621007, Tamil Nadu, India
[c] Department of Chemistry, College of Science, Taif University, P.O. Box 11099, Taif 21944, Saudi Arabia
[d] Department of Physics, Karpagam Academy of Higher Education (Deemed to be University), Coimbatore 641021, Tamil Nadu, India
[e] Department of Physics, Smart Nanomaterial Research Laboratory, Government City PG College (A), Osmania University, Hyderabad, TG 500002, India
[f] Sede Vallenar, Universidad de Atacama, Av. Costanera # 105, Vallenar 1612178, Chile
[g] Departamento de Química, Facultad de Ciencias Naturales, Matemáticas y del Medio Ambiente, Universidad Tecnológica Metropolitana, Las Palmeras 3360, 7800003 Ñuñoa, Región Metropolitana, Chile
[h] Saveetha School of Engineering, Saveetha Institute of Medical and Technical Sciences (SIMATS), Chennai 602105, Tamil Nadu, India
[i] Department of Civil Engineering, Yeungnam University, Gyeongsan, 38541, Republic of Korea
[j] Centre for Research Impact & Outcome, Chitkara University Institute of Engineering and Technology, Chitkara University, Rajpura, 140401, Punjab, India

ARTICLE INFO

Keywords:
Photocatalysis
Terbium-doped U-TiO_2
UV-C and Solar light
Dye breakdown
Microbial disinfection

ABSTRACT

The relentless discharge of synthetic dyes from industrial sectors poses severe threats to aquatic ecosystems and public health due to their toxicity, persistence, and resistance to conventional treatment methods. Addressing these concerns, we developed a urea-modified terbium-doped titanium dioxide (Tb-U-TiO_2) photocatalyst via a sol–gel technique followed by thermal treatment. The synergistic effect of Tb^{3+} doping and urea modification enhanced crystallinity, extended visible-light absorption, and suppressed charge recombination. Comprehensive characterization using XRD, FT-IR, Raman, FE-SEM, HR-TEM, XPS, PL, and UV-DRS confirmed structural, morphological, and optical improvements. Photocatalytic activity was assessed by degrading Acid Black 1 (AB 1) under UV-C and Reactive Red 120 (RR 120) under natural sunlight. The optimized 0.4 wt% Tb-U-TiO_2 catalyst achieved complete degradation of AB 1 and 96.87% removal of RR 120, outperforming unmodified U-TiO_2. Kinetic studies revealed pseudo-first-order behaviour, and parameter optimization established ideal pH and catalyst loading conditions. GC–MS analysis identified key intermediates and proposed a degradation pathway. Radical scavenging experiments confirmed that $O_2^{\bullet-}$ and h^+ were the dominant active species. Beyond dye removal, the catalyst exhibited strong antibacterial activity against both Gram-positive and Gram-negative strains, demonstrating its dual functionality in pollutant degradation and microbial disinfection. The material also showed excellent stability and reusability over multiple cycles with negligible performance loss. Overall, this work presents Tb-U-TiO_2 as a cost-effective, solar-responsive, and multifunctional photocatalyst with significant promise for next-generation integrated wastewater treatment and environmental protection.

1. Introduction

The commercialization of dyes reached its peak as various sectors, involving garments, groceries, drugs, scientific fields, and commercial uses kicked off to adopt them extensively [1]. Researchers throughout the world were looking at ways to manage water contaminants including crop residue, factory waste, infectious microbes, and everyday waste [2]. Synthetic dyes are chemically engineered colorants widely used in textiles, cosmetics, and food due to their vibrant hues and stability [3]. They are broadly classified into ionic (cationic/anionic) and nonionic types based on their charge and application method. Cationic dyes bind strongly to negatively charged surfaces like acrylic, while an-

* Corresponding authors.
E-mail addresses: drskannanphy@gmail.com (K. S), kbalu@us.es (K. Balu).

https://doi.org/10.1016/j.surfin.2025.107909
Received 8 July 2025; Received in revised form 10 October 2025; Accepted 16 October 2025
2468-0230/© 20XX

CORRECTED PROOF

Note: Low-resolution images were used to create this PDF. The original images will be used in the final composition.

ionic dyes adhere to positively charged materials such as cotton and wool via electrostatic interactions [4,5]. Nonionic dyes, lacking charge, rely on hydrogen bonding and van der Waals forces, making them suitable for neutral surfaces like polyester. Disperse and vat dyes are common examples of nonionic dyes [6]. However, synthetic dye effluents significantly threaten water quality, reducing light penetration and harming aquatic life [7]. Azo dyes (–*N*═*N*–), in particular, are of concern due to their toxicity and persistence in ecosystems. They can disrupt photosynthesis, oxygen levels, and aquatic biodiversity [8]. Thus, sustainable dyeing methods and stricter regulations are crucial for environmental protection. The elimination of pigments from commercial by-products is imperative for the reason of the possibility of tumor-causing and mutation-triggering effects, which present significant risks to biodiversity and community health [9,10]. Moreover, dye-laden industrial effluents significantly hinder light penetration in aquatic environments, disrupting photosynthetic activity, depleting dissolved oxygen levels, and endangering aquatic ecosystems [11]. The advent of nanotechnology has revolutionized wastewater treatment and recycling, offering advanced approaches including membrane filtration, enhanced sludge processing, reverse osmosis, flocculation, and light-driven photocatalytic systems [12]. Traditional approaches such as physical adsorption and biological treatments often fall short in effectively eliminating dyes from wastewater, particularly reactive dyes [13]. Due to their complex molecular architecture and the presence of multiple functional groups, these dyes establish strong covalent bonds with substrates. This structural rigidity significantly impedes their breakdown, making them resistant to conventional removal techniques [14,15]. To tackle the limitations of conventional treatment methods, advanced oxidation processes (AOPs) have emerged as effective alternatives for eliminating soluble dyes that resist standard removal techniques [16]. Among these, photocatalysis stands out as a powerful strategy, utilizing light energy in combination with a catalyst to initiate and accelerate the oxidative breakdown of organic contaminants [17]. This method harnesses photo-induced reactive species to efficiently degrade persistent dye molecules into non-toxic end products [18]. Numerous studies have focused on the development of solid-phase photocatalysts like ZnO, TiO_2, CdS, and WO_3, aiming to enhance the breakdown of dye pollutants [19,20]. These semiconductor materials are being extensively explored for their ability to harness light energy and trigger efficient degradation of complex dye molecules in contaminated water systems. Photocatalysts are generally solid-state materials, widely studied metal oxides, for example, titanium dioxide (TiO_2) and zinc oxide (ZnO), that interact with reactants present in liquid or gas phases [21]. When exposed to light, these solids absorb energy, exciting electrons and creating charge pairs generated by light. The generated charge carriers diffuse toward the catalyst surface, where they initiate oxidation and reduction reactions with molecules that are adsorbed onto the material's surface [22,23]. For practical applications, titanium dioxide (TiO_2) is considered one of the most efficient photocatalysts, owing to its remarkable attributes. It is environmentally friendly, highly efficient in facilitating electron transfer, and economically viable [24]. Moreover, TiO_2 exhibits exceptional stability under both chemical and thermal conditions, making it a durable and reliable choice for various photocatalytic processes [25]. Upon light activation, it generates electron–hole pairs that interact with organic contaminants, initiating reactions that break down and eliminate these pollutants. Despite its advantages, TiO_2 faces limitations including a lack of visible light absorption, limited efficiency in degrading certain pollutants, and reduced effectiveness in the presence of interfering substances [26]. Consequently, enhancing titanium oxide's capability to selectively degrade highly toxic contaminants under visible light is a critical research focus [27]. Terbium (Tb), a rare earth element, has partially filled 4f orbitals and vacant 5d orbitals that allow it to absorb visible light effectively. These unique electronic properties enable terbium not only to enhance catalytic processes but also to function as a catalyst itself [28]. When incorporated into TiO_2 as a dopant, terbium significantly enhances the material's luminescence, making it particularly attractive for photocatalytic applications. Known for its strong green emission due to intra-4f electronic transitions within the 400–600 nm range, terbium plays a crucial role in modifying TiO_2's optical characteristics. Its presence leads to the extension of the absorption edge into the red region, enabling better utilization of visible light. Additionally, terbium helps to hinder the recombination of photogenerated charge carriers, resulting in enhanced charge separation and superior photocatalytic activity. As a result, terbium-doped TiO_2 stands out as a highly effective photocatalyst for environmental remediation and solar-driven applications [29–31].

Recent studies have reported the use of advanced composite materials for photocatalytic degradation. For instance, S. tul Shafa et al. [32] investigated a copper and terbium co-doped nickel ferrite ($CuxNi_{1-x}TbyFe_{2-y}O_4$, x, y = 0.1) integrated with MXene (CTNF/MXene) for the efficient degradation of Congo Red (CR), Crystal Violet (CV), and Diclofenac Sodium (DS) under visible light. Results demonstrated that the incorporation of terbium and copper significantly decreased the crystallite size and band gap energy, improved absorption in the visible light region, and suppressed the recombination of electron–hole pairs, thereby enhancing photocatalytic performance. The incorporation of MXene as a co-catalyst further facilitated electron trapping and improved photocatalytic efficiency. Enhanced surface area and pollutant adsorption due to terbium's complexation ability contributed to higher degradation efficiencies: CR (91 %), CV (77 %), and DS (81 %). Overall, CTNF/MXene outperformed NF, CNF, TNF, and CTNF alone in photocatalytic performance under visible light. In recent investigations, L. Lal et al., [33] investigated the photocatalytic degradation of malachite green dye employing Tb^{3+}-doped nickel sulfide nanoparticles, targeting the mitigation of environmental issues caused by synthetic dye pollution. The catalyst underwent detailed analysis through XRD, SEM, TEM, PL, XPS, and UV–Vis techniques. The research reported that 94 % degradation was attained within 90 min, significantly influenced by pH and the presence of additives. Transition-metal ions and inorganic oxidants facilitated degradation, in contrast to inorganic anions which hindered it. Additionally, an artificial neural network (ANN) model accurately predicted degradation behavior, underscoring the potential of ANN in optimizing photocatalytic systems for wastewater treatment. Recent work by N. AlMasoud et al., [34] focused on the photocatalytic breakdown of carcinogenic dyes like crystal violet and rhodamine B using lithium nickel ferrite-based nanocomposites. Ferrites, known for their strong visible light absorption and efficient charge carrier mobility, were synthesized along with terbium-doped variants and combined with graphitic carbon nitride (g-C_3N_4) via sol-gel and ultrasonication methods. The $LiNiTbFe_2O_4$@g-C_3N_4 composite exhibited superior photocatalytic activity, degrading 86 % of crystal violet and 83 % of rhodamine B within 120 min. Structural and optical characterizations confirmed enhanced charge separation and a reduced bandgap of 1.87 eV. These findings highlight the potential of rare-earth-doped ferrite/g-C_3N_4 composites for effective wastewater treatment. NS Arul et al., [35] synthesized CeO_2/Tb_2O_3 nanotubes (NTs) using a surfactant-free co-precipitation method. Structural and compositional characterizations via HRTEM, XPS, and EDAX confirmed the formation of CeO_2/Tb_2O_3 NTs. The photocatalytic activity was assessed through the breakdown of methylene blue (MB) exposed to visible light. The reaction proceeded according to pseudo-first-order kinetics, with rate constants of 0.0134 min^{-1} for CeO_2 NPs and 0.0317 min^{-1} for CeO_2/Tb_2O_3 NTs. The nanotubes exhibited a high photodegradation efficiency of 93 % within 75 min, outperforming pure CeO_2 NPs (66 %). The observed enhancement arises from facilitated charge separation and enhanced sensitivity to visible light.

In this study, urea-modified terbium-doped titanium dioxide (Tb-U-TiO_2) photocatalysts were synthesized via a sol-gel method followed by thermal treatment. Their photocatalytic performance was assessed

CORRECTED PROOF

through the degradation of Acid Black 1 under UV-C light and Reactive Red 120 under natural sunlight. The influence of Tb doping and urea modification on structural and optical properties was systematically investigated. GC–MS analysis was conducted to identify degradation intermediates and propose a possible degradation pathway. Additionally, the antibacterial activity of the optimized catalyst was evaluated against selected bacterial strains. The catalyst exhibited excellent photocatalytic efficiency, reusability, and antibacterial performance, demonstrating its potential for wastewater treatment and disinfection applications.

2. Experimental procedure

2.1. Chemical ingredients

High-purity analytical reagent (AR) grade chemicals were used throughout the study, with no need for further purification. The primary reagents included 2-propanol ($CH_3CH(OH)CH_3$; CAS No: 67–63–0, MW: 60.1 g/mol), titanium isopropoxide ($C_{12}H_{28}O_4Ti$; CAS No: 546–68–9, MW: 284.22 g/mol), terbium nitrate pentahydrate ($Tb(NO_3)_3{\cdot}5H_2O$; CAS No: 57,584–27–7, MW: 435.02 g/mol), urea (CH_4N_2O; CAS No: 57–13–6, MW: 60.0553 g/mol) and glacial acetic acid (CH_3COOH; CAS No: 64–19–7, MW: 60.05 g/mol) were employed. Deionized water and ethanol served as solvents during both the synthesis and purification processes. The structural formula and absorption maxima of the azo dyes Acid Black 1 and Reactive Red 120 are detailed in **Table S1**.

2.2. Fabrication of urea-mediated Tb-TiO_2 and U-TiO_2

The fabrication process commenced by creating Solution A, where 20 mmol (1.201 g) of urea was dissolved in 40 mL of 2-propanol. Subsequently, 2 mL of glacial acetic acid, 5 mL of deionized water, and 30 mg of terbium nitrate pentahydrate were added stepwise to the solution. In parallel, Solution B was formed by mixing 10 mL of titanium isopropoxide with 30 mL of 2-propanol until fully dissolved. Afterward, Solution A and Solution B were blended together and stirred intensively for 1 h to achieve a uniform mixture. The combined solution was placed into a 100 mL Teflon-lined stainless-steel autoclave and underwent hydrothermal processing at 130 °C for 12 h inside a hot air oven. After cooling to ambient temperature, the precipitate was separated through filtration, rinsed thoroughly three times using a 1:1 ethanol–water solution, and then dried at 90 °C for 10 h. The obtained dry powder was finely ground using a mortar and pestle, placed in a silica crucible, and calcined at 600 °C for 5 h in a muffle furnace. Following gradual cooling to ambient temperature, the resultant Tb-doped U-TiO_2 photocatalyst containing 0.4 wt % Tb was retrieved and stored for later use. For comparative analysis, catalysts with varying terbium content were synthesized by following the same protocol using 15 mg (0.2 wt %) and 60 mg (0.8 wt %) of terbium nitrate pentahydrate. The pristine U-TiO_2 sample was synthesized under the same conditions, omitting terbium doping.

2.3. Characterization techniques

A comprehensive set of analytical techniques was employed to investigate the structural, optical, and surface characteristics of the synthesized photocatalysts. Powder X-ray diffraction (PXRD) measurements were carried out using a PANalytical X'Pert PRO diffractometer equipped with a 15 KVA UPS, within a 2θ range of 20°–80°, to confirm phase purity and crystal structure. Fourier-transform infrared spectroscopy (FT-IR) (Thermo Fisher Nicolet iS5) was used to identify surface functional groups, while Raman spectroscopy (Image Spectrograph STR, 500 mm focal length) provided high-resolution vibrational information with a spectral resolution of 1/0.6 cm^{-1} per pixel and a flat field of 27 × 14 mm. The optical properties were studied using a Jasco V-650 UV–Vis spectrophotometer covering 200–800 nm, along with diffuse reflectance spectroscopy (DRS) to evaluate absorption behavior. Photoluminescence (PL) spectra were recorded at 77 K on a Varian Cary Eclipse spectrometer to probe charge carrier recombination and electronic transitions. Additional UV–Vis absorption analysis was performed using a Perkin-Elmer Lambda 35 spectrometer to validate light–matter interactions. For morphological studies, field-emission scanning electron microscopy (FE-SEM, Carl Zeiss Sigma 300) was employed, offering up to 1.0 nm resolution at 15 kV and operability between 0.02–30 kV. Elemental mapping and compositional analysis were obtained through energy-dispersive X-ray spectroscopy (EDS) integrated into the FE-SEM system. Further insight into nanoscale structure was achieved by high-resolution transmission electron microscopy (HR-TEM, JEOL JEM-2100 Plus, Japan), supported by selected area electron diffraction (SAED) to verify crystallinity. Finally, the elemental states and surface chemical composition were determined by X-ray photoelectron spectroscopy (XPS, PHI Versaprobe III), providing crucial information on oxidation states and bonding environments.

2.4. Evaluation of photocatalytic performance

The photocatalytic degradation of the azo dye Acid Black 1 (AB 1) was carried out using a Heber multi-lamp photoreactor (Model: HML-COMPACT-LP-MP88). The reactor was equipped with four low-pressure mercury UV-C lamps, each rated at 8 W, emitting predominantly at a wavelength of 254 nm. For the photocatalytic degradation studies, 20 mg of the catalyst, either undoped U-TiO_2 or terbium (Tb)-doped U-TiO_2, was dispersed in 100 mL of Acid Black 1 (AB 1) dye solution at a concentration of 20 ppm and neutral pH (pH 7). To ensure equilibrium between adsorption and desorption of dye molecules on the catalyst surface, the suspension was magnetically stirred in the dark for 30 min. After this equilibration step, the suspension was transferred into cylindrical quartz reaction tubes (inner diameter: 2.5 cm; length: 37 cm) and kept under constant stirring in dark conditions until the photocatalytic reaction was initiated by irradiation. The dye suspension was subsequently subjected to UV-C light irradiation. At regular intervals of 10 min, 3 mL aliquots were extracted from the reaction mixture for further analysis. Each sample was centrifuged using a REMI-R-8C centrifuge to filter out the solid photocatalyst, and the clear solution was analyzed using UV–Visible spectrophotometry to monitor the degradation progress. The experiments were performed in triplicate. The same experimental procedure was repeated under natural sunlight irradiation (950 W/m^2; humidity ≈ 70 %; wind speed ≈ 12–16 km/h) for RR 120 dye degradation, and samples collected at 30-min intervals. The absorbance of each sample was recorded to assess the light-driven catalytic efficiency of the materials under solar light conditions. The relative decrease in azo dye concentration (%) was determined using Eq. (1).

$$\text{Catalytic Breakdown efficiency of the azo dyes } (\%) = \frac{C_0 - C_t}{C_0} \times 100 \quad (1)$$

Here, C_0 denotes the starting concentration of the azo dyes, namely Acid Black 1 (AB 1) and Reactive Red 120 (RR 120) and C_t denotes the concentration after irradiation for time t.

Detailed methodologies pertaining to the collection of test pathogens, assessment of antibacterial activity via the disc diffusion method, and analysis of degradation pathway via GC–MS (sample preparation method) are provided in the Supporting Information

CORRECTED PROOF

3. Results and discussion

3.1. Microstructural and light-absorption insights

3.1.1. Structural phase identification

X-ray diffraction (XRD) analysis was performed to examine the crystal structures of the pristine U-TiO_2 and terbium-doped U-TiO_2 (Tb–U-TiO_2) photocatalysts, with the results presented in Fig. 1. For the undoped U-TiO_2 sample, prominent diffraction peaks appeared at 2θ angles of 25.68° (101), 36.18° (103), 38.04° (004), 39.91° (112), 48.27° (200), 54.23° (105), 55.38° (211), 62.49° (213), 63.21° (204), 68.97° (116), 70.75° (220), 74.04° (107), 75.33° (215), and 76.42° (301). These characteristic peaks correspond well with the standard JCPDS card No. 21–1272, confirming that the material crystallizes in the anatase phase possessing a tetragonal crystal structure [36,37]. This form of TiO_2 is well-known for its excellent photocatalytic performance due to its high surface area and effective charge carrier mobility. When U-TiO_2 was doped with terbium (Tb), the XRD patterns showed no additional peaks, indicating that the anatase phase remains stable even after doping. However, the peaks became slightly broader and shifted marginally towards higher angles. This broadening suggests a decrease in crystallite size or the presence of increased lattice strain, while the shift in peak position points to subtle distortions in the crystal lattice due to the introduction of Tb ions. These structural changes confirm that Tb^{3+} ions have successfully entered the TiO_2 lattice. Due to the ionic radius of Tb^{3+} (≈0.92 Å) is larger than that of Ti^{4+} (≈0.61 Å), this substitution introduces lattice strain and can result in the emergence of oxygen vacancies to equalize charge imbalance. Such oxygen vacancies actively improve photocatalytic properties by improving charge separation and increasing surface active sites. Doping U-TiO_2 with terbium adjusts its crystal structure and electronic properties, resulting in Tb-U-TiO_2 exhibiting superior photocatalytic performance through increased light absorption and more effective separation of photo-induced charge carriers.

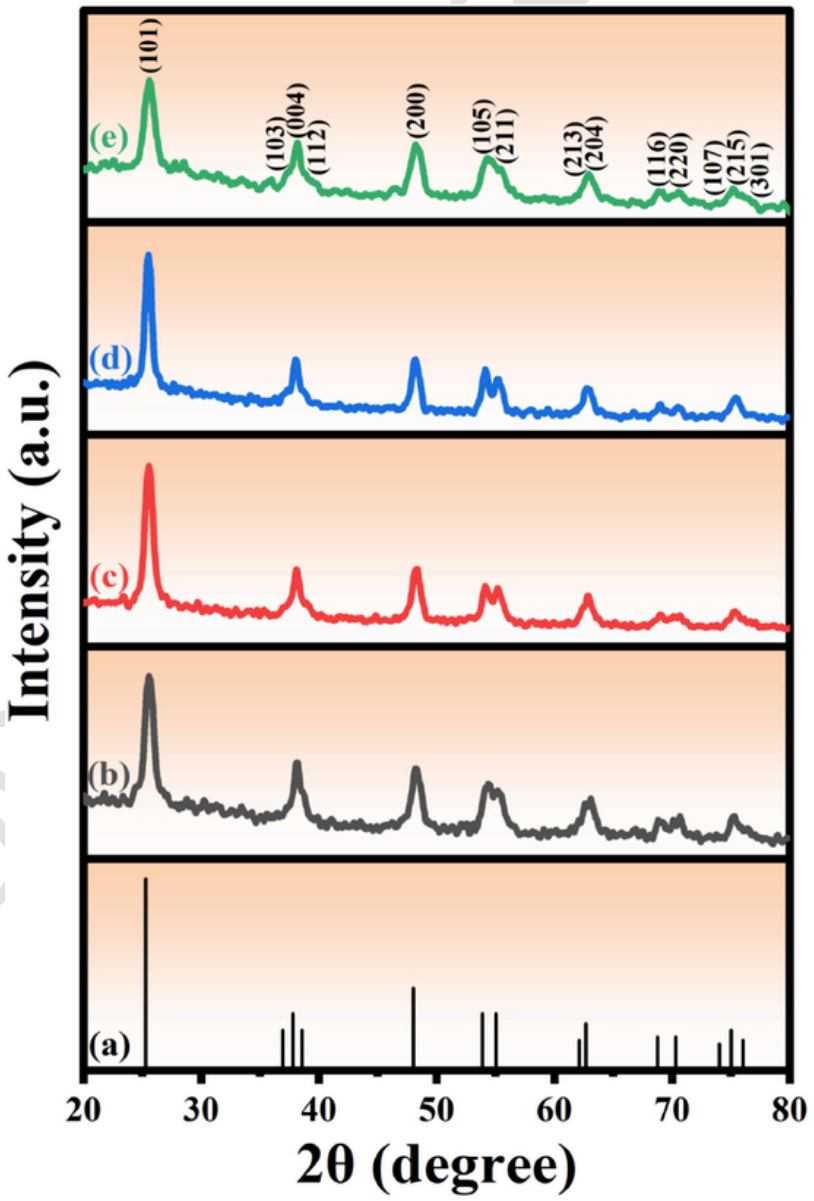

Fig. 1. X-ray diffraction (XRD) spectra of (a) standard anatase TiO_2 (JCPDS card No. 21–1272), (b) undoped TiO_2 (U-TiO_2), and Tb-doped U-TiO_2 photocatalysts with terbium concentrations of (c) 0.2 wt %, (d) 0.4 wt %, and (e) 0.8 wt %.

3.1.2. Functional group identification

The FT-IR spectra of both undoped U-TiO_2 and Tb-doped U-TiO_2 nanoparticles, presented in Fig. 2a, provide important insights into the structural composition and surface properties of the synthesized catalysts within the wavenumber range of 400–4000 cm^{-1}. In the region of lower wavenumber (400–800 cm^{-1}), a noticeable absorption band is present, which can be attributed to the flexural vibrations of O–Ti–O bonds. This characteristic confirms the development of crystalline TiO_2, demonstrating a well-organized lattice arrangement in the catalyst structure [38]. At 1640 cm^{-1}, a distinct absorption peak emerges, attributed to the bending vibrations of surface hydroxyl (–OH) groups, which play a vital role in photocatalytic activity by facilitating pollutant adsorption and triggering the reaction process [39,40]. Moreover, a broad absorption band observed in the 3300–3700 cm^{-1} corresponds to the stretching vibrations of water molecules physically adsorbed on the catalyst surface. The interaction with hydroxyl groups emphasizes the hydrophilic nature of the TiO_2 surface [41]. Importantly, the Tb-doped U-TiO_2 samples exhibit these key spectral features consistently, although slight shifts in peak positions are evident, implying that terbium incorporation does not disrupt the fundamental structure and surface chemistry of the TiO_2 matrix.

3.1.3. Vibrational modes analysis

Fig. 2b displays the Raman spectra for both the undoped TiO_2 (U-TiO_2) and terbium-doped TiO_2 (Tb-U-TiO_2) catalysts. Characteristic peaks for the anatase phase of TiO_2 appear at 143.69, 394.90, 517.96, and 639.36 cm^{-1}, corresponding to the $E_{g(1)}$, $B_{1g(1)}$, $A_{1g}+B_{1g(2)}$, and $E_{g(2)}$ vibrational modes, respectively [42]. The peak observed at approximately 143.69 cm^{-1} corresponds to the symmetric stretching vibrations of oxygen atoms in the O–Ti–O bonds, whereas the peak near 394.90 cm^{-1} is due to the symmetric bending vibrations of the O–Ti–O mode. The 517.96 cm^{-1} band signifies antisymmetric bending vibrations, and the 639.36 cm^{-1} peak reflects symmetric stretching, all linked to the fundamental vibrational modes of anatase TiO_2. Upon doping with Tb, noticeable changes in the Raman spectra occur. Specifically, peak broadening and enhanced intensity are observed at doping levels of 0.2 wt % and 0.4 wt % Tb, with further broadening at 0.8 wt % Tb, indicating subtle lattice disturbances induced by the Tb incorporation. However, the absence of any additional peaks confirms that the intrinsic vibrational structure of anatase TiO_2 remains unaltered. This broadening effect is a hallmark of lattice distortion and variations in crystallinity, which validate the effective embedding of Tb ions into the TiO_2 framework. Such modifications can positively influence photocatalytic efficiency by promoting better charge carrier separation and surface reactivity, all while preserving the structural integrity of the anatase phase.

3.1.4. Charge carrier recombination study

Photoluminescence (PL) spectroscopy was employed to evaluate the charge carrier dynamics, Specifically, the spatial separation and recombination dynamics of light-generated electron-hole pairs, in both undoped TiO_2 (U-TiO_2) and terbium-doped TiO_2 (Tb-U-TiO_2) photocata-

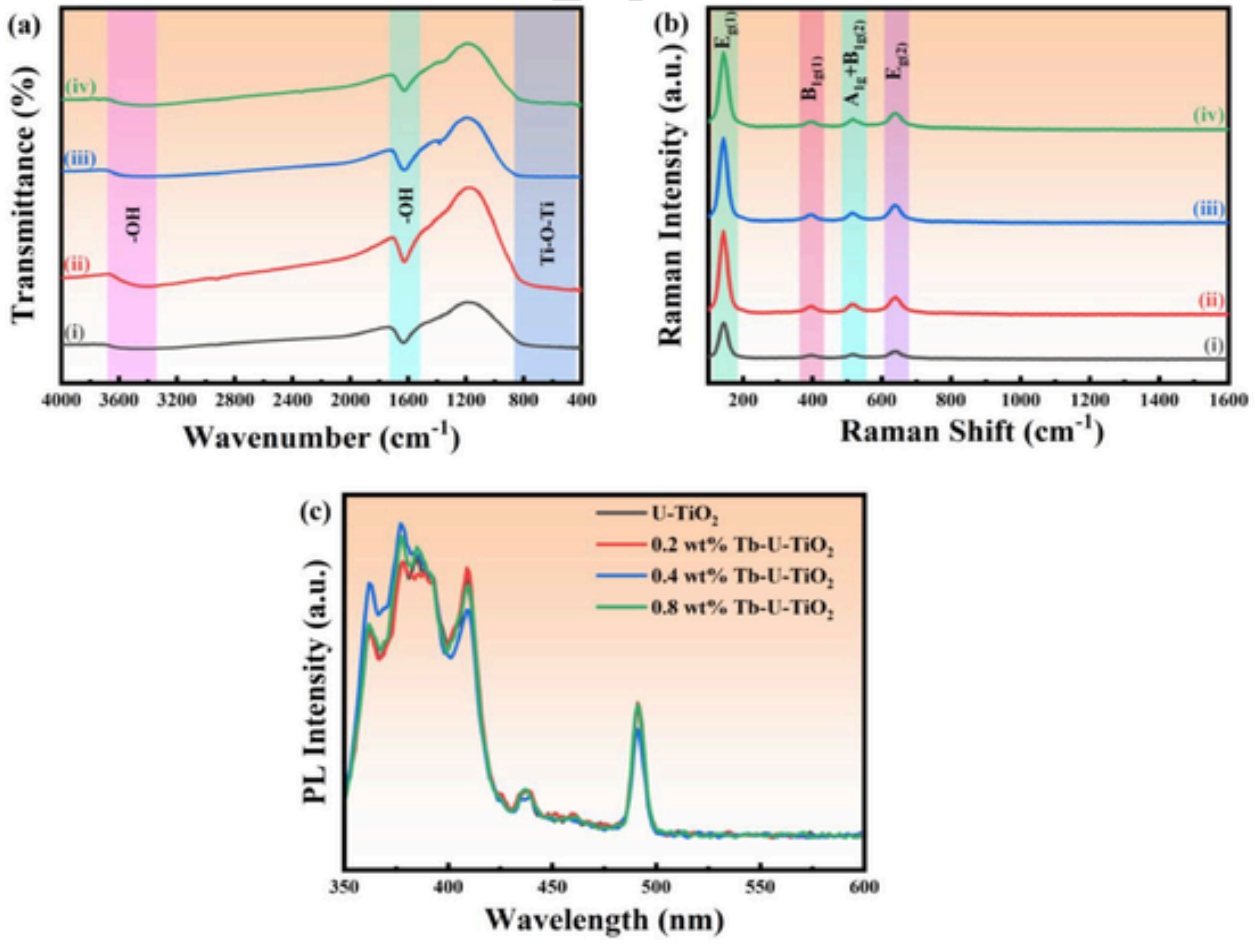

Fig. 2. (a) FT-IR spectra, (b) FT-Raman spectra, and (c) PL spectra of (i) undoped urea-derived TiO_2 (U-TiO_2) and terbium (Tb)-doped U-TiO_2 photocatalysts at different doping concentrations: (ii) 0.2 wt %, (iii) 0.4 wt %, and (iv) 0.8 wt %.

lysts. As depicted in Fig. 2c, the PL spectra of these samples revealed distinct emission peaks at wavelengths of 362, 378, 385, 408, 438, 461, and 491 nm [45,46]. The undoped U-TiO_2 sample exhibited relatively lower PL intensity, suggesting suppressed charge carrier recombination and a longer lifetime of photogenerated electrons and holes, which is generally favourable for photocatalysis. Interestingly, the Tb-doped U-TiO_2 photocatalyst displayed higher PL intensities, particularly at a doping concentration of 0.4 wt %, which typically indicates increased recombination. However, despite the higher PL signal, the Tb-doped samples showed improved photocatalytic activity. This apparent contradiction may be attributed to the role of Tb^{3+} ions in introducing localized energy states or surface defects that enhance visible-light absorption and facilitate interfacial charge transfer, thereby compensating for the recombination loss. Thus, the improved photocatalytic performance may stem not solely from reduced recombination, but from a combination of enhanced light harvesting, effective charge separation at active sites, and increased generation of reactive species. Each PL peak corresponds to specific electronic transitions and defect states within the TiO_2 lattice. For instance, the emission at 378 nm originates from the band edge, while the 408 nm peak is attributed to shallow trap states [47,48]. The 461 nm emission signifies surface-related defects involving surface-level traps or lattice oxygen vacancies, and the pronounced peak at 491 nm is associated with oxygen-depleted regions, also known as F-centers [49,50]. As noted earlier in the XRD analysis, the substitution of Ti^{4+} ions by Tb^{3+} within the TiO_2 crystal framework leads to a charge disparity, arising from the mismatch in their oxidation states. To compensate, the system forms oxygen-deficient sites, which have a pivotal role in enhancing photocatalytic activity by serving as active sites for charge separation and reactive species generation. Interestingly, the majority of emission maxima appear in the ultraviolet region (300–400 nm), with the most intense response observed for the 0.4 wt % Tb-doped TiO_2 sample. This optimal doping level not only enhances PL emission but also slightly shifts the peak positions, suggesting modifications in the local electronic environment. These observations demonstrate that embedding of Tb^{3+} not only tunes the defect structure but also significantly boosts the sustained segregation of photogenerated electron-hole pairs by the catalyst, leading to superior performance under UV-C light compared to the undoped TiO_2 and other Tb doping concentrations.

3.1.5. Optical band gap determination

Fig. 3a presents the UV–Vis absorption spectra, which were employed to assess the light-harvesting efficiency of both pure and Tb-doped TiO_2 photocatalysts. The corresponding optical band gaps of the fabricated photocatalysts were estimated using the Kubelka-Munk function, F(R), based on established mathematical expressions provided in the subsequent equations [43,44].

$$(F(R)h\nu)^n = A(h\nu - Eg) \quad (2)$$

$$F(R) = \frac{(1-R)^2}{2R} \quad (3)$$

Here, R denotes the material's diffuse reflectance, and hυ signifies the photon energy, with h representing Planck's constant and υ the frequency of the incoming light. The factor A serves as a proportionality constant, capturing the material's inherent optical properties. The exponent n depends on the type of semiconductor band gap, where n equals 2 for direct band gap materials and ½ for those with an indirect band gap. In semiconductor physics, a common method to determine a material's band gap energy (E_g) involves examining its optical absorption behavior. This is typically done using a Kubelka-Munk plot, where the value of E_g is determined by extrapolating the linear portion of the plot of $(F(R)h\upsilon)^n$ to the x-axis (photon energy axis). For direct band gap semiconductors like TiO_2, $n = 2$ is used in the calculation. As shown in Fig. 3b, the undoped U-TiO_2 catalyst exhibits a band gap energy of 3.32 eV. Upon doping with terbium

(Tb), variations in the band gap were observed depending on the dopant concentration. Specifically, the band gap energies for Tb-doped U-TiO_2 were estimated to be 3.30 eV, 3.36 eV, and 3.35 eV for Tb concentrations of 0.2 wt %, 0.4 wt %, and 0.8 wt %, respectively (Fig. 3c-e). Notably, a slight narrowing of the band gap at lower level (0.2 wt %) was observed, while the band gap widened marginally at the higher concentration. This tuning of the band gap through Tb incorporation signifies a meaningful shift in the absorption cutoff, shifting toward visible light, which is crucial for enhancing photocatalytic performance. Among the synthesized materials, the 0.4 wt % Tb-doped U-TiO_2 exhibited enhanced visible light absorption across the entire visible spectrum. This improved light-harvesting capability enables the catalyst to absorb a broader range of sunlight wavelengths, thereby increasing the generation of electron–hole pairs. As a result, more reactive species are formed, which significantly enhances the degradation of pollutants under light irradiation.

3.2. Particle morphology investigation

3.2.1. Nanoscale surface morphology and nanostructure visualization analysis

Field emission scanning electron microscopy (FE-SEM) facilitated the examination of surface and particle structure of the prepared photocatalysts, namely pristine U-TiO_2 and 0.4 wt % Tb-doped U-TiO_2. The corresponding FE-SEM micrographs captured at various magnifications appear in Fig. 4a–f. As indicated in Fig. 4a–c, the bare U-TiO_2 exhibits aggregated yet well-dispersed spherical nanoparticles. These clusters are indicative of a relatively uniform growth habit, although some degree of agglomeration is evident, likely arising from interparticle interactions during the thermal treatment. Despite the aggregation, the spherical shape is maintained throughout the sample, reflecting a consistent synthetic process.

Upon doping with terbium (0.4 wt %), the FE-SEM scans in Fig. 4d–f reveal that the spherical morphology is largely preserved, confirming that Tb incorporation does not cause major alterations to the native morphology of TiO_2 particles. Remarkably, the Tb-U-TiO_2 micrographs display regions with smoother and more homogeneous surface textures compared to the undoped sample. This textural refinement suggests an improved dispersion and integration of Tb ions within the TiO_2 matrix, potentially facilitating a more uniform nucleation and growth during synthesis. Moreover, both pristine and Tb-doped samples exhibit particle sizes within the nanometer scale, which is crucial for photocatalytic applications. The nanoscale size guarantees an elevated surface area relative to volume, thereby enhancing the concentration of active sites that facilitate efficient light absorption and surface redox processes. As a result, the FE-SEM analysis confirms that Tb doping at 0.4 wt % maintains the morphological integrity of U-TiO_2 while subtly enhancing surface uniformity. This morphological stability, coupled with nanoscale particle size, is expected to contribute positively to the photocatalytic performance of the material by optimizing light absorption and charge carrier dynamics.

The FE-SEM micrographs of Tb-U-TiO_2 with other doping concentrations (0.2 wt % and 0.8 wt %) are presented in **Fig. S1** (see Supporting information). Specifically, **Fig. S1a–c** corresponds to 0.2 wt % Tb-U-TiO_2, while **Fig. S1d–f** represents 0.8 wt % Tb-U-TiO_2. In both cases, the surface morphology reveals densely packed, unevenly distributed clusters composed of aggregated spherical nanoparticles, indicating that Tb doping does not significantly alter the overall spherical morphology but may influence the degree of particle agglomeration.

3.2.2. Elemental distribution studies

Energy dispersive spectroscopy (EDS) and elemental mapping, were performed in conjunction with FE-SEM and HR-TEM analyses, offered a

CORRECTED PROOF

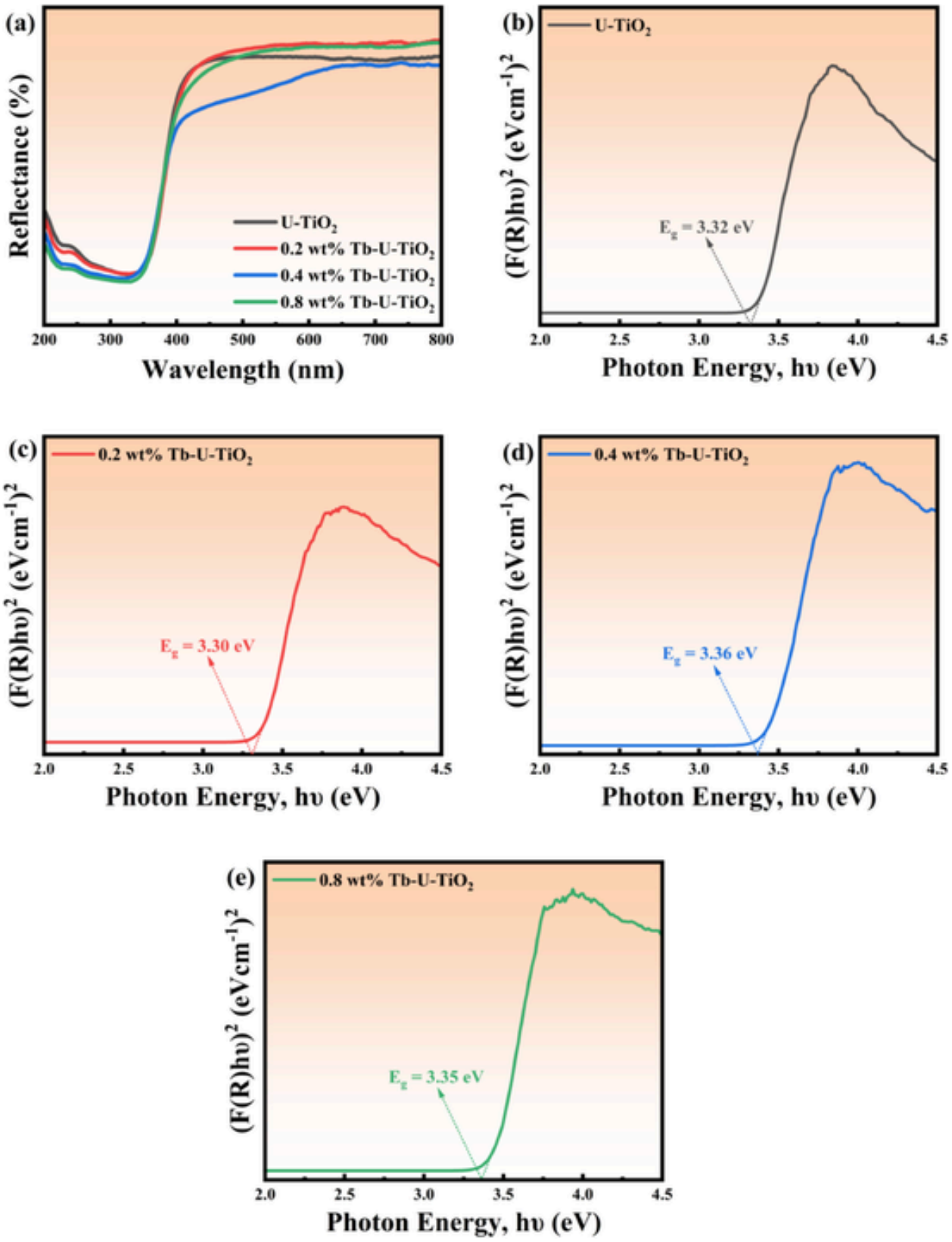

Fig. 3. (a) UV–Vis diffuse reflectance spectra with their associated Kubelka-Munk (KM) plots for (b) pristine U-TiO_2 and Tb-doped U-TiO_2 photocatalysts at doping levels of (c) 0.2 wt %, (d) 0.4 wt %, and (e) 0.8 wt %.

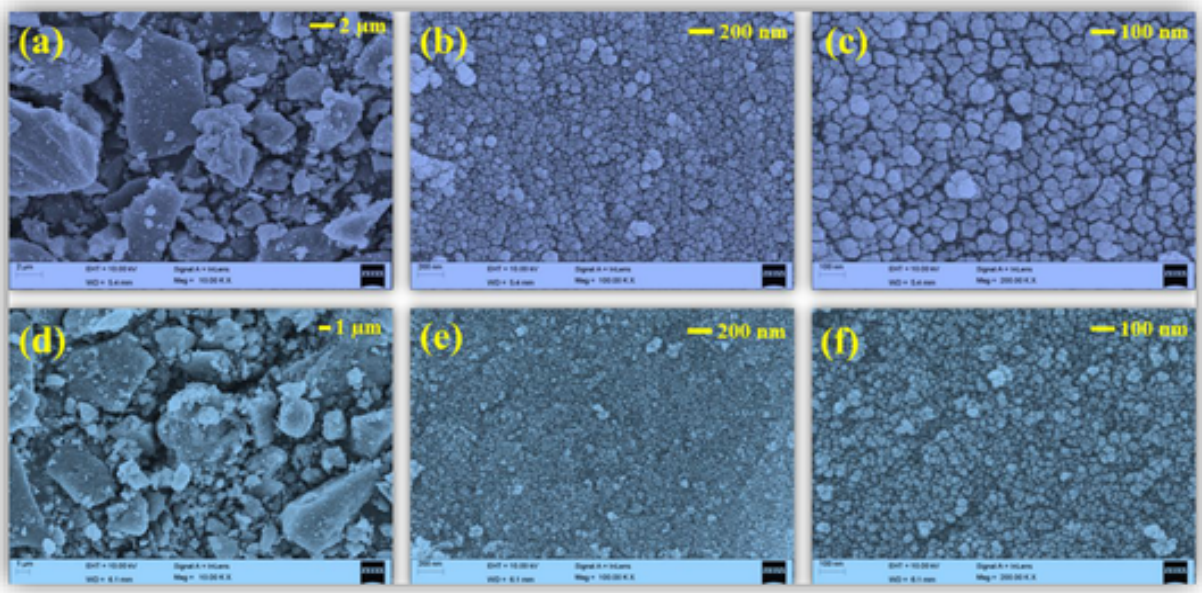

Fig. 4. FE-SEM scans of (a-c) U-TiO_2 and (d-e) 0.4 wt % Tb-doped U-TiO_2 photocatalysts.

thorough assessment of the synthesized U-TiO_2 and 0.4 wt % Tb-U-TiO_2 photocatalysts (refer to **Fig. S2** and **Tables S2** & **S3** in the Supporting Information). The EDS spectra distinctly revealed the elemental makeup of the samples, emphasizing the spatial arrangement of key elements. In the case of U-TiO_2, strong signals for titanium (Ti) and oxygen (O) were detected within the energy intervals of 0–1 keV and 4.2–5 keV, respectively, aligning well with the typical TiO_2 composition, as illustrated in **Fig. S2a**. In the case of the Tb-doped sample (0.4 wt % Tb-U-TiO_2), additional signals were observed in the 1–1.8 and 6–8 keV regions, confirming the successful presence of terbium (Tb) along with Ti and O (**Fig. S2b**). These spectral features affirm that Tb was successfully integrated into the TiO_2 lattice, a crucial modification aimed at enhancing its photocatalytic efficiency. The EDS findings substantiate the effective doping of Tb into the TiO_2 matrix, which is instrumental in boosting its functional performance under photocatalytic conditions. Similarly, for the Tb-doped samples (0.2 wt % and 0.8 wt % Tb-U-TiO_2), characteristic peaks were detected in the 1–1.8 keV and 6–8 keV regions, corresponding to the Tb, along with signals for Ti and O (**Figs. S3a** and **S3b**). These results confirm the successful incorporation of Tb into the TiO_2 lattice. **Tables S4** and **S5** present the elemental composition, expressed in terms of weight (%) and atomic (%), for the 0.2 wt % and 0.8 wt % Tb-U-TiO_2 photocatalysts, respectively. Moreover, elemental mapping results presented in **Fig. S4** depict a homogeneous distribution of all detected elements in both the undoped U-TiO_2 and 0.4 wt % Tb doped U-TiO_2 samples. This uniform elemental dispersion is vital for achieving consistent photocatalytic activity, as it ensures widespread availability of active sites and facilitates more efficient interaction with pollutants. Overall, the complementary data from EDS and elemental mapping confirm the successful fabrication and even distribution of Tb into the TiO_2 structure, underlining its promise for advanced photocatalytic applications.

3.2.3. HR-TEM analysis

Fig. 5 and Fig. S5 present a comprehensive morphological and structural characterization of the 0.4 wt % Tb-doped U-TiO_2 photocatalyst through transmission electron microscopy (TEM) and high-resolution TEM (HR-TEM) techniques. The low- and intermediate-magnification TEM images (Fig. 5a and b), taken from various regions of the sample, exhibit a heterogeneous distribution of nearly spherical nanoparticles. These observations indicate a uniform nanoscale morphology with some agglomeration. Higher-resolution structural details are provided in the HR-TEM images (Fig. 5c and h), where well-defined lattice fringes are clearly visible, demonstrating the high crystallinity of the material. These lattice fringes correspond to specific crystallographic planes of TiO_2, indicating that Tb^{3+} ions have been successfully introduced into the TiO_2 lattice without disrupting the overall crystalline framework. To further explore the crystallographic ordering and domain orientation, fast Fourier transform (FFT) analyses were conducted on selected regions of the HR-TEM images (highlighted by yellow squares and red circles in (Fig. 5c and h). The resulting FFT patterns (Fig. 5d and i) reveal well-ordered diffraction spots, confirming the periodic atomic arrangement and the presence of highly crystalline domains.

To enhance the clarity of specific lattice information, frequency-masked FFT regions were subjected to inverse fast Fourier transform (IFFT) analysis, as shown in Fig. 5e and k. The corresponding IFFT images (Fig. 5g and l) effectively filter out background noise, providing a clearer visualization of the lattice structure and allowing for accurate measurement of interplanar spacings and fringe orientations. The lattice spacing measurements, derived from intensity profiles of the IFFT images (Fig. 5f and j), provide additional insight into the structural integrity of the sample. Two distinct D-spacing values were identified: approximately 0.363 nm and 0.400 nm. The 0.363 nm spacing aligns well with the (101) plane of anatase TiO_2, indicating that the anatase phase is preserved post-doping. The slightly larger spacing of 0.400 nm is attributed to lattice expansion likely caused by the partial substitution of Ti^{4+} with larger Tb^{3+} ions, which induces localized strain and modifies the Ti–O bond lengths within the lattice. Overall, the HR-TEM and associated FFT/IFFT analyses confirm that the 0.4 wt % Tb-doped U-TiO_2 photocatalyst retains excellent crystallinity, exhibits nanoscale morphological uniformity, and undergoes minor lattice expansion due to dopant incorporation. These structural features are critical in enhancing the material's photocatalytic efficiency by promoting effective charge separation and maintaining robust crystallographic order.

3.2.4. Surface analysis and chemical state determination

Fig. S6 and Fig. 6 presents the X-ray photoelectron spectroscopy (XPS) data, providing detailed insights into the elemental composition

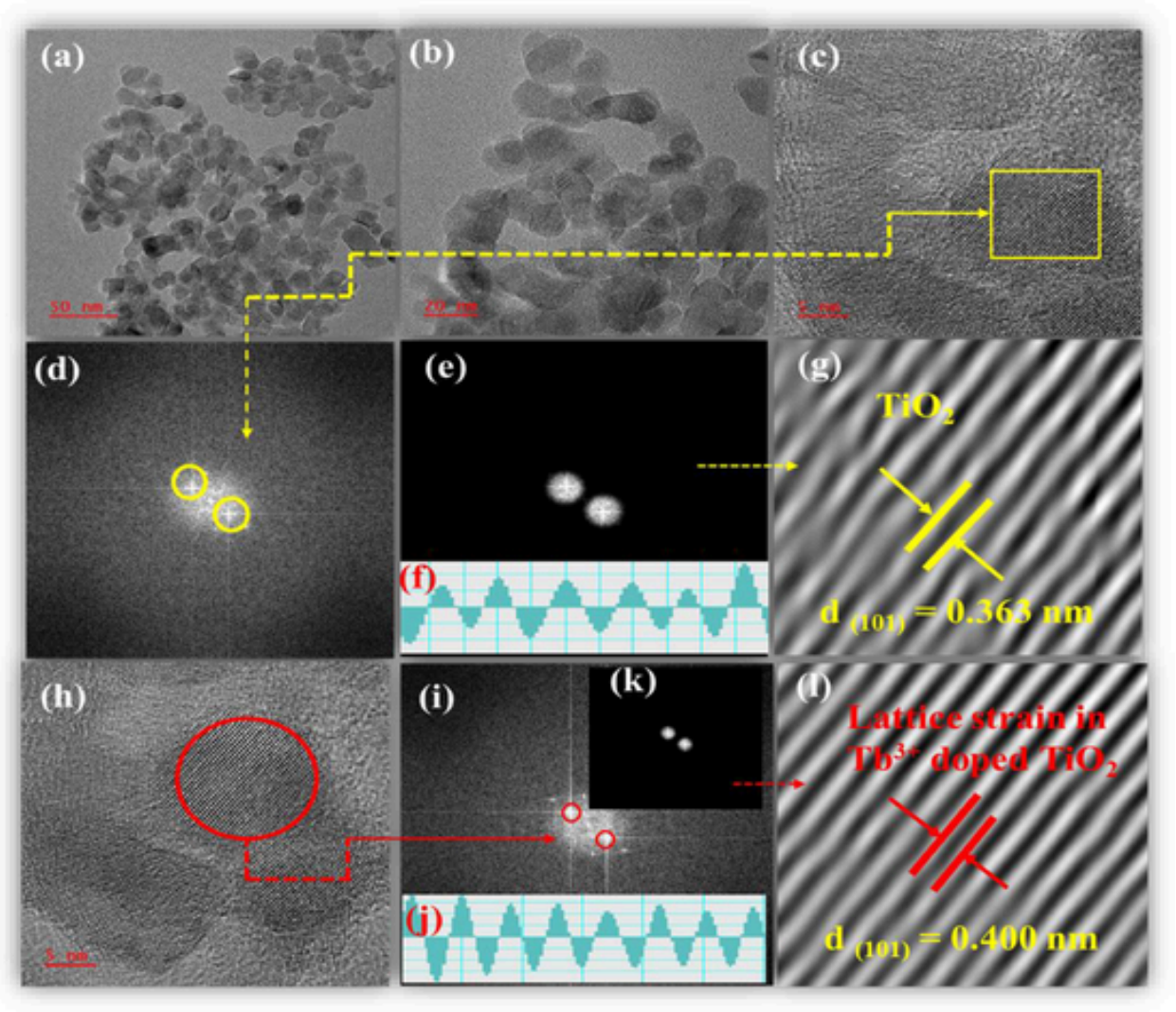

Fig. 5. (a, b) TEM images, (c and h) HR-TEM images of 0.4 wt % Tb-doped U-TiO_2 photocatalyst, (d and i) corresponding FFT, (e and k) mask area, (f and j) profile of IFFT, (g and l) IFFT images with crystalline planes of Tb-doped U-TiO_2.

and oxidation states present in the bare U-TiO_2 and 0.4 wt % Tb-doped U-TiO_2 photocatalysts. **Fig. S6** presents the X-ray photoelectron spectroscopy (XPS) spectra of the U–TiO_2 photocatalyst, providing detailed insights into its elemental composition and chemical states. The survey spectrum (**Fig. S6a**) confirms the presence of Ti, O, and N elements, indicating the successful fabrication of the urea-modified TiO_2 material. The high-resolution Ti 2p spectrum (**Fig. S6b**) displays two prominent peaks located at 457.86 eV and 463.66 eV, which correspond to Ti $2p_{3/2}$ and Ti $2p_{1/2}$, respectively [51,52]. These values are consistent with the characteristic binding energies of Ti^{4+}, confirming that titanium in the sample exists predominantly in its tetravalent oxidation state. The O 1 s spectrum (**Fig. S6c**) shows two peaks at 529.08 eV and 531.21 eV [53]. The former is attributed to lattice oxygen within the TiO_2 crystal framework, while the latter corresponds to surface hydroxyl groups and adsorbed oxygen species. The coexistence of these oxygen environments is known to play an important role in photocatalysis by promoting charge separation and facilitating the generation of reactive radicals. The N 1 s spectrum (**Fig. S6d**) exhibits a single peak at 399.37 eV, which is assigned to substitutional nitrogen incorporated into the TiO_2 lattice through Ti–N–O bonding. This indicates that nitrogen atoms derived from the decomposition of urea effectively replaced some oxygen sites in the lattice. The absence of higher binding energy peaks suggests a relatively uniform nitrogen configuration, with no significant contribution from oxidized nitrogen species. Such substitutional nitrogen doping is beneficial for narrowing the band gap of TiO_2 and extending its visible-light absorption, thereby enhancing its photocatalytic activity.

Fig. 6 shows the individual spectra of 0.4 wt % Tb-doped U-TiO_2 examining the binding energy regions linked to Ti, O, Tb, and N (sourced from urea), confirming their successful integration and distinct chemical states within the composite matrix. The survey spectrum (Fig. 6a) displays distinct peaks corresponding to Ti 2p, O 1 s, Tb 3d, and N 1 s, confirming the successful fabrication of the Tb-U-TiO_2 nanocomposite and the effective incorporation of all constituent elements into the material. The high-resolution Ti 2p spectrum (Fig. 6b) exhibits well-defined peaks at 457.90 eV and 463.71 eV, which are attributed to Ti $2p_{3/2}$ and Ti $2p_{1/2}$, respectively. The observed binding energy values are indicative of Ti existing mainly in its +4 oxidation state, confirming the dominance of its tetravalent form within the material matrix, an important factor contributing to the photocatalytic efficiency of TiO_2 [54,55]. The O 1 s high-resolution spectrum displays two distinct peaks at 529.12 eV and 531.23 eV, indicating the presence of multiple oxygen species within the sample (Fig. 6c). The peak appearing at the lower binding energy of 529.12 eV corresponds to

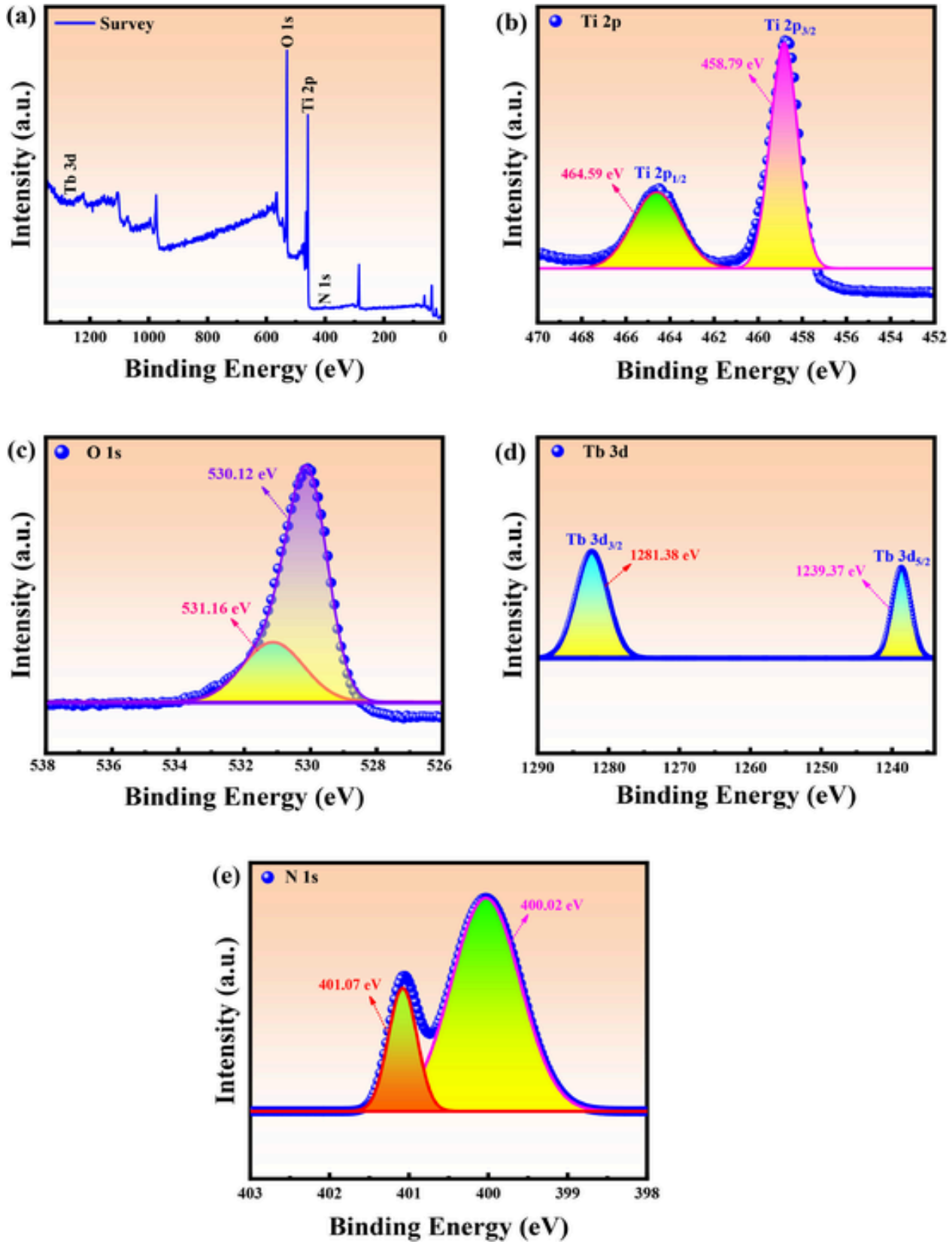

Fig. 6. XPS spectra of 0.4 wt % Tb-U-TiO_2 photocatalyst showcasing (a) the survey scan, (b) Ti 2p region, (c) O 1 s region, (d) Tb 3d region, and (e) N 1 s region.

oxygen atoms integrated within the TiO_2 crystal lattice., whereas the higher energy peak at 531.23 eV is attributed to surface-associated oxygen and hydroxyl components. These oxygen species are essential for enhancing photocatalytic efficiency by facilitating effective charge carrier separation and aiding the formation of reactive intermediate species [43].

The detailed XPS spectrum focusing on the Tb 3d region (Fig. 6d) reveals two well-resolved peaks at binding energies of 1239.89 eV and 1275.25 eV, which correspond to the Tb $3d_{5/2}$ and Tb $3d_{3/2}$ spin–orbit components, respectively. This splitting arises due to spin–orbit coupling and is characteristic of the 3d core level of terbium. The observed binding energies indicate that terbium exists predominantly in the +3 oxidation state (Tb^{3+}), typically found in oxide environments. The detection of these peaks confirms the effective embedding of terbium within the TiO_2 crystal structure or on its surface, where it can act as an electron trap, thereby improving charge carrier partition and boosting the overall photocatalytic performance of the composite material. The XPS analysis of the N 1 s region (Fig. 6e) displays two separate peaks at binding energy values of 400.09 eV and 404.69 eV, shedding light on the chemical environment of nitrogen within the Tb-doped TiO_2 matrix. The peak observed at 400.09 eV signifies the presence of interstitial nitrogen atoms that have been effectively integrated into the TiO_2 framework, most likely introduced via nitrogen doping during the thermal breakdown of urea. Meanwhile, the higher energy peak at 404.69 eV suggests the presence of oxidized nitrogen species (NOx, nitro groups), which are typically formed during synthesis due to surface interactions between nitrogen intermediates and metal ions. These nitrogen species play a significant role in altering the electronic configuration of TiO_2 or Tb, potentially enhancing the photocatalytic performance. The XPS analysis definitively verifies the effective integration of Tb^{3+} ions into the TiO_2 lattice, rather than the formation of separate Tb-based oxide phases. This is strongly supported by the lack of supplementary peaks related to elevated oxidation states or secondary terbium oxides. The ionic radius of Tb^{3+} (≈0.92 Å) is notably larger than that of Ti^{4+} (≈0.61 Å), and its substitution into the TiO_2 crystal framework induces local lattice distortion and strain.

The Urea doping shows a notable distinction between the two samples arises in the nitrogen spectra. For bare U–TiO_2, the N 1 s region (**Fig. S6d**) shows a single peak centered at 399.37 eV, corresponding to substitutional nitrogen incorporated into the TiO_2 lattice through Ti–N–O bonding. The absence of higher binding energy contributions suggests a relatively uniform nitrogen configuration. In contrast, the Tb–U–TiO_2 spectrum (Fig. 6e) displays two distinct peaks at 400.09 eV and 404.69 eV. The peak at 400.09 eV indicates interstitial nitrogen species introduced into the lattice during synthesis, whereas the higher-energy feature at 404.69 eV is attributed to oxidized nitrogen species (NOx or nitro groups) formed via surface interactions. The coexistence of multiple nitrogen states in the Tb–doped sample suggests that Tb incorporation facilitates nitrogen stabilization in diverse chemical environments, leading to electronic structure modifications and enhanced light-harvesting capability. Overall, the XPS results clearly demonstrate that while both samples contain Ti^{4+}, lattice oxygen, surface hydroxyl groups, and nitrogen species, the Tb–U–TiO_2 nanocomposite exhibits a richer nitrogen chemistry and additional Tb^{3+} states. These features are expected to enhance photocatalytic performance by creating new electronic states, improving charge trapping, and extending visible-light absorption compared to bare U–TiO_2.

To compensate for the charge imbalance introduced by the aliovalent substitution (Tb^{3+} replacing Ti^{4+}), oxygen vacancies are likely generated. These oxygen vacancies are particularly significant; they serve as active centers that enhance the photocatalytic performance by facilitating more efficient charge separation and providing reactive sites for pollutant degradation [56,57]. Moreover, the structural tuning brought about by Tb doping not only modifies the crystallinity of TiO_2 but also alters its electronic band structure, thereby broadening light absorption into the visible region. Collectively, these findings demonstrate that the doping of terbium into the TiO_2 matrix enhances its photocatalytic properties, making Tb–TiO_2 an excellent prospect for applications in environmental clean-up. The synergistic effects of lattice strain, oxygen vacancies, and improved electronic interactions all contribute to a more efficient and robust photocatalyst.

3.2.5. Electrochemical impedance spectroscopy (EIS) analysis and photocatalytic implications

The Nyquist plots of pristine U-TiO_2 and 0.4 wt % Tb-doped U-TiO_2 are presented in **Fig. S7**, to evaluate the charge transfer resistance and interfacial properties of the photocatalysts. The impedance response of both samples exhibits semicircular arcs, which are characteristic of charge transfer processes occurring at the electrode–electrolyte interface. Notably, the arc diameter of the Tb-doped U-TiO_2 sample is significantly smaller compared to that of bare U-TiO_2, indicating a lower charge transfer resistance (Rct). This reduction in resistance demonstrates that terbium incorporation enhances the separation and mobility of photogenerated charge carriers by suppressing electron–hole recombination.

In addition, the decreased impedance response of Tb-U-TiO_2 suggests improved interfacial charge transport efficiency, which can be attributed to the introduction of Tb^{3+} ions creating localized energy levels within the TiO_2 band structure. These defect states promote electron trapping and facilitate charge migration, thereby reducing recombination losses. The enhanced electrical conductivity and faster interfacial charge transfer are consistent with the superior photocatalytic activity observed for Tb-doped U-TiO_2 compared to undoped U-TiO_2. Thus, the EIS results clearly confirm that Tb doping plays a vital role in reducing charge transfer resistance, improving conductivity, and enhancing the overall photocatalytic efficiency of U-TiO_2.

4. Light-driven catalytic performance evaluation

4.1. UV-C light-induced photodegradation of acid black 1 azo dye

To assess the photocatalytic prowess of the synthesized materials, dye degradation experiments were meticulously conducted using a 20 ppm solution of AB 1 degradation under ultraviolet-C (UV-C) light exposure. In each trial, an amount of 20 mg of the synthesized photocatalyst was homogeneously blended with 100 mL of dye solution, maintained at a neutral pH (pH 7), ensuring uniform interaction between the catalyst and dye molecules. Prior to light exposure, the reaction mixture was stirred in complete darkness to establish adsorption–desorption equilibrium. This crucial step confirmed that any subsequent dye removal could be confidently attributed to photocatalytic activity rather than passive physical adsorption. As anticipated, no notable degradation occurred during this phase, underscoring the indispensability of light in activating the photocatalytic pathway. Upon UV-C illumination, the catalyst materials began to absorb photon energy, initiating electronic excitation across the band gap, causing the generation of charge carriers (e^-/h^+ pairs), which served as the primary driving force for advanced redox reactions. These charge carriers subsequently facilitated the emergence of oxidative species, including potent hydroxyl and superoxide radicals. These highly reactive intermediates launched an aggressive assault on the AB 1 dye molecules, breaking down their complex structures through oxidative pathways. The progression of dye degradation was meticulously tracked using UV–Visible spectroscopy by monitoring the prominent absorption maximum of AB 1 located at approximately 618 nm. A consistent decline in peak intensity was recorded as irradiation continued, reflecting a dynamic and efficient decomposition of the dye. Remarkably, after just 60 min of UV-C exposure, the absorbance peak nearly disappeared, an unequivocal indicator of outstanding photocatalytic performance. This dramatic reduction signifies not only high dye removal efficiency but also suggests

CORRECTED PROOF

substantial mineralization of the pollutant, as vividly illustrated in Fig. 7.

Fig. 7a–e shows the time-dependent UV–Vis absorption spectra for the degradation of the target dye solution under UV-C light irradiation using different photocatalysts: (a) U-TiO_2, (b) 0.2 wt % Tb-U-TiO_2, (c) 0.4 wt % Tb-U-TiO_2, (d) 0.8 wt % Tb-U-TiO_2, and (e) TiO_2 (without urea). The characteristic absorption peak of the dye is observed around 618 nm, and its gradual decrease with increasing irradiation time indicates progressive photodegradation. Among the samples, bare TiO_2 (Fig. 7e) exhibited the least photocatalytic efficiency, with only a slight reduction in absorbance even after 60 min of irradiation. This is attributed to the fast recombination of photogenerated electron–hole pairs and poor light absorption capability. U-TiO_2 (Fig. 7a) showed improved degradation compared to TiO_2, which can be ascribed to the modification effect of urea that induces oxygen vacancies and defect sites, thereby enhancing charge separation and light response. In the case of Tb-doped samples (Fig. 7b–d), the photocatalytic activity further improved with Tb incorporation. The 0.2 wt % Tb-U-TiO_2 sample (Fig. 7b) displayed moderate activity, whereas the 0.4 wt % Tb-U-TiO_2 (Fig. 7c) demonstrated the most significant decrease in absorbance, indicating superior photocatalytic degradation efficiency. This enhancement can be attributed to the optimal Tb doping, which introduces trap states that facilitate efficient electron transfer and suppress charge recombination. However, when the Tb content was increased to 0.8 wt % (Fig. 7d), the activity slightly decreased, likely due to excess Tb ions acting as recombination centers that hinder charge carrier mobility.

Fig. 8a clearly illustrates the time-dependent photocatalytic degradation of Acid Black 1 (AB 1) dye under UV-C light irradiation using U-TiO_2 and Tb-doped U-TiO_2 photocatalysts. Among the samples, 0.4 wt % Tb-U-TiO_2 demonstrates the most remarkable performance, achieving nearly complete mineralization (≈100 %) of AB 1 within 60 min. This result is substantially higher than that of pristine U-TiO_2, which achieved only 29.74 % degradation under identical conditions. The significant improvement in Tb-doped samples is attributed to efficient dissociation and migration of photogenerated charge carriers, wherein Tb^{3+} ions act as electron traps, suppress recombination, and thereby prolong charge carrier lifetimes. The relative concentration profiles (C_t/C_0) shown in Fig. 8b further corroborates this observation. A sharp decline in C_t/C_0 for the 0.4 wt % Tb-U-TiO_2 sample indicates accelerated dye degradation, whereas U-TiO_2 maintains a relatively high Ct/C0 value, even after prolonged irradiation, reflecting its poor catalytic activity. The intermediate doping levels (0.2 wt % and 0.8 wt %) also display improved activity compared to undoped U-TiO_2, but their efficiencies remain below that of the optimally doped 0.4 wt % sample.

The kinetic behavior of AB 1 degradation, analyzed using the pseudo-first-order model (Fig. 8c), further validates the catalytic performance. A strong linear correlation between $-\ln(C_t/C_0)$ and irradiation time was obtained for all samples, confirming the pseudo-first-order nature of the degradation process. The kinetic rate constant (k) for pristine U-TiO_2 was the lowest at 0.00563 min^{-1} (R^2 = 0.92515), consistent with its limited activity. Upon Tb doping, the reaction kinetics improved significantly. The 0.2 wt % Tb-U-TiO_2 sample exhibited an enhanced k value of 0.03286 min^{-1} (R^2 = 0.96402), while the 0.4 wt % Tb-U-TiO_2 sample showed the highest k of 0.05675 min^{-1} (R^2 = 0.9508), confirming its superior charge separation and efficient ROS generation. However, further increasing the Tb content to 0.8 wt % reduced the rate constant to 0.03532 min^{-1}, likely due to excess Tb^{3+} ions introducing recombination centers or saturating surface-active sites, thereby diminishing efficiency despite a strong correlation (R^2 = 0.96373). The final degradation percentages after 60 min are summarized in Fig. 8d, where the performance order is as follows: 0.4 wt % Tb-U-TiO_2 (≈100 %) > 0.8 wt % Tb-U-TiO_2 (87.6 %) ≈ 0.2 wt % Tb-U-TiO_2 (86.01 %) > *U*-TiO_2 (29.74 %). The degradation rates per unit catalyst mass for U–TiO_2, 0.2 wt % Tb–U–TiO_2, 0.4 wt % Tb–U–TiO_2, and 0.8 wt % Tb–U–TiO_2 were found to be 48.26, 139.45, 162.24, and 142.08 μmol g^{-1} h^{-1}, respectively. This trend clearly highlights that moderate Tb doping (specifically 0.4 wt %) provides an optimal balance between enhanced light absorption, efficient charge separation, and sufficient surface reaction sites. In contrast, excessive Tb loading reduces activity by creating recombination centers and hindering active site availability Overall, the comprehensive analysis of Fig. 8a–d demonstrates that Tb doping significantly enhances the photocatalytic performance of U-TiO_2, with 0.4 wt % emerging as the most effective catalyst for AB 1 degradation under UV-C light irradiation.

4.2. Natural solar irradiation-induced photocatalytic breakdown of RR 120

Performance assessment of the doped and undoped catalysts under natural sunlight was systematically investigated. In this experiment, a 20 mg dose of catalyst: comprising both undoped and 0.4 wt % terbium-doped U-TiO_2, which was uniformly introduced into an RR 120 dye solution (50 ppm) with a volume of 100 mL. The mixture was stirred to ensure homogeneous dispersion before exposure to sunlight. Periodic sampling every 30 min followed by UV–Vis spectroscopy enabled detailed monitoring of the degradation process. As evidenced by **Fig. S8**, the absorbance spectra revealed a steady reduction in the dye's signature peak at 525 nm, confirming the catalyst's photocatalytic activity. The continuous decrease in peak intensity with time reflected the progressive breakdown of the dye molecules during solar-driven photoreactions. The study demonstrated remarkable photocatalytic degradation of the azo dye RR 120 under sunlight, highlighting the potential of the synthesized catalysts for environmental cleanup applications. After irradiation, the bare U-TiO_2 catalyst achieved a degradation efficiency of 80.83 %, while the 0.4 wt % Tb-doped U-TiO_2 significantly outperformed it, achieving 96.87 % degradation, as depicted in Fig. 9a. This notable improvement underscores the enhanced photocatalytic capabilities imparted by terbium doping. Fig. 9b presents the normalized absorbance spectra (C_t/C_0) over time, showing a consistent decline in the dye's absorbance intensity with prolonged sunlight exposure, clear evidence of progressive molecular degradation.

To better understand the reaction dynamics, the degradation data were modelled employing the Langmuir-Hinshelwood approach, as demonstrated in Fig. 9c. The correlation coefficients (R^2) were found to be 0.94629 for the bare catalyst and 0.80496 for the Tb-doped variant, indicating strong linearity and fitting. Moreover, the calculated rate constants were 0.01093 min^{-1} for bare U-TiO_2 and 0.02092 min^{-1} for 0.4 wt % Tb-U-TiO_2, confirming a more rapid degradation rate in the presence of the doped catalyst. Fig. 9d illustrates the final degradation performance at the 180-minute mark, where the Tb-doped sample exhibited an additional 16.04 % removal of RR 120 compared to its undoped counterpart. For RR 120 under sunlight, the degradation rates per unit catalyst mass were determined to be 55.0 μmol g^{-1} h^{-1} for U–TiO_2 and 65.9 μmol g^{-1} h^{-1} for 0.4 wt % Tb–U–TiO_2, indicating enhanced photocatalytic activity with Tb doping. These results emphasize the superior efficiency and faster photocatalytic response of Tb-U-TiO_2 under natural sunlight, positioning it as a highly effective and environmentally sustainable material to detoxify wastewater containing dye compounds.

4.3. Impact of pH conditions and photocatalyst amount

To optimize the light-activated removal of AB 1 dye using Tb-doped U-TiO_2 photocatalyst under UV-C irradiation, a detailed investigation was undertaken to explore the effects of starting pH and catalyst quantity, as depicted in Fig. 10. These two operational parameters are critical in determining the success rate of the degradation, influencing both the surface charge dynamics and the active site availability of the photocatalyst. As shown in Fig. 10a, the photocatalytic performance was assessed across a pH range of 3 to 11. A marked dependence on pH was observed, with degradation efficiency showing a clear trend. At acidic

CORRECTED PROOF

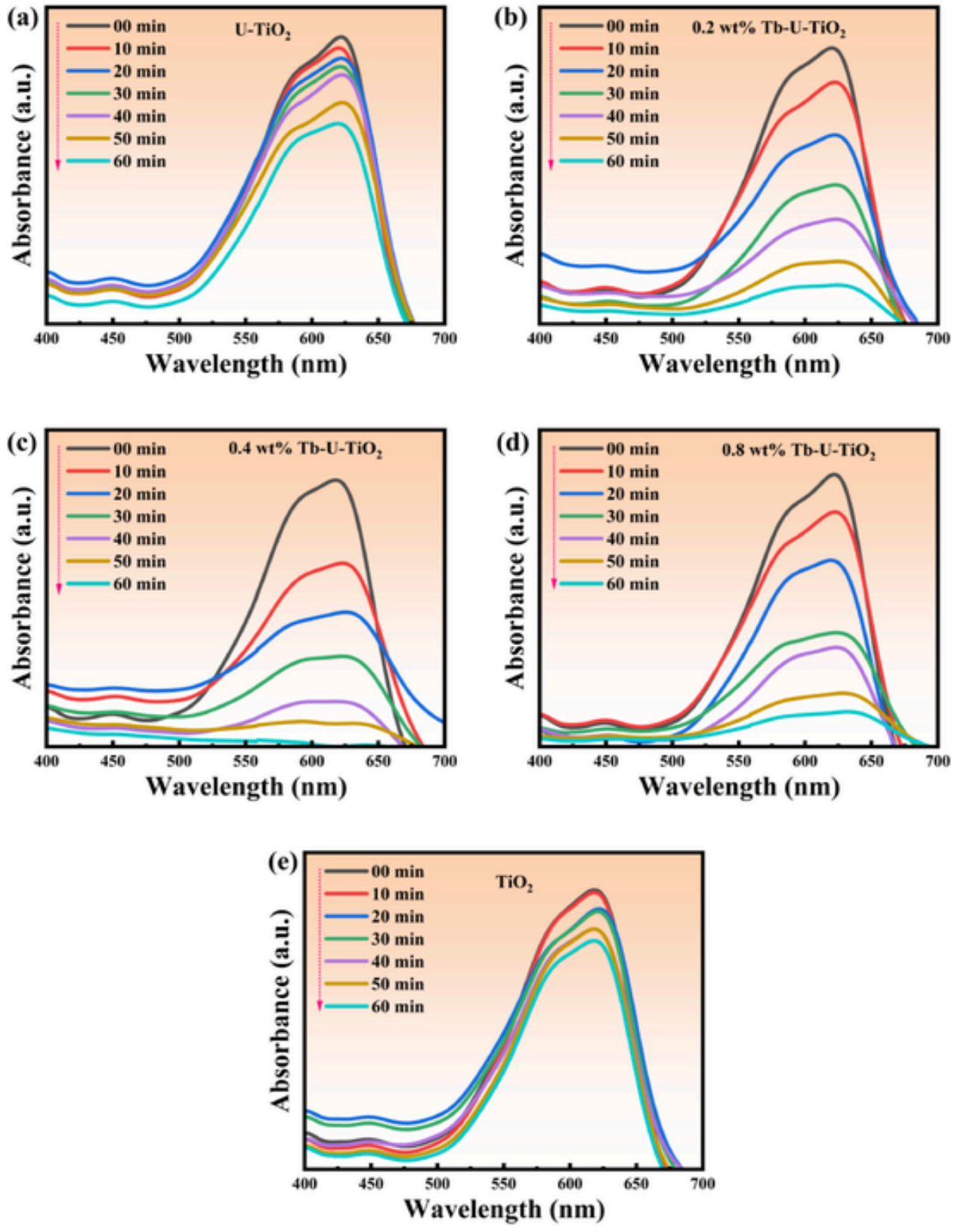

Fig. 7. UV–Vis absorption spectra showing the progressive elimination of Acid Black 1 (AB 1) dye exposed to UV-C light irradiation at various time intervals using (a) Pristine U-TiO_2, (b) 0.2 wt %, (c) 0.4 wt %, (d) 0.8 wt % Tb-doped U-TiO_2 and (e) TiO_2 photocatalysts [Experimental conditions: catalyst dosage = 20 mg, dye concentration = 20 ppm, and pH = 7].

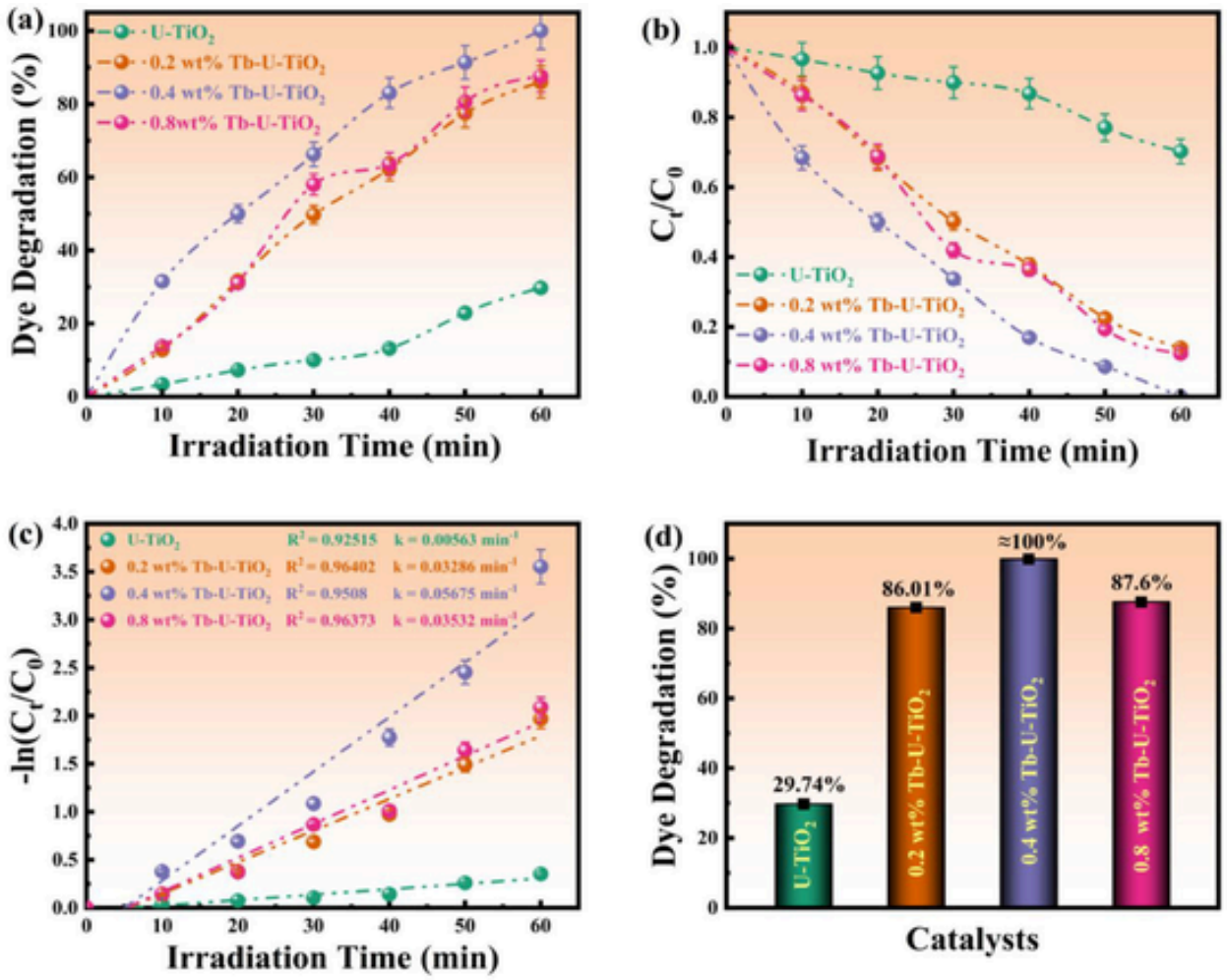

Fig. 8. (a) Photocatalytic degradation of Acid Black 1 (AB 1) dye under UV-C irradiation, comparing pristine U-TiO_2 with Tb-doped U-TiO_2 catalysts; (b) evolution of normalized dye concentration (C_t/C_0) over irradiation time highlighting degradation dynamics; (c) linearized pseudo-first-order kinetic plots demonstrating reaction rate constants; and (d) a comparative summary of photocatalytic efficiencies across all samples following 60 min of UV-C exposure.

pH 3, the system exhibited a relatively low degradation rate of 24.47 %, which moderately improved to 49.58 % at pH 5. The top efficiency in degradation, approaching ≈100 %, was achieved at neutral pH 7, highlighting the optimal surface interactions and charge interaction synergy between dye molecules and catalyst under neutral conditions. Beyond pH 7, the efficiency declined gradually to 86.96 % at pH 9 and 79.72 % at pH 11. These results suggest that at strongly acidic or basic conditions, the catalyst surface may undergo changes (such as protonation or deprotonation), adversely affecting its photocatalytic activity. The neutral pH likely facilitates an ideal balance between surface stability and charge interaction, maximizing the generation and transfer of reactive oxygen species.

The point of zero charge (pHpzc) is a fundamental surface property that determines the charge characteristics of a photocatalyst in aqueous suspensions and strongly influences its interaction with charged pollutants. To determine the pHpzc of Tb–U–TiO_2, the ΔpH method was employed, where the difference between the initial and final pH values (ΔpH) was plotted against the initial pH (pHi), as illustrated in **Fig. S9**. The intersection of the curve with the zero line (ΔpH = 0) provides the pHpzc value of the catalyst. As shown in the plot, the pHpzc of Tb–U–TiO_2 was determined to be 6.88. This indicates that the catalyst surface is predominantly positively charged at pH < 6.88, due to protonation of surface hydroxyl groups ($\equiv$Ti–OH + H^+ → $\equiv$Ti–OH_2^+). Conversely, at pH > 6.88, the surface becomes negatively charged, as deprotonation dominates ($\equiv$Ti–OH → $\equiv$Ti–O^- + H^+). This surface charge behavior is crucial in explaining the photocatalytic degradation efficiency of anionic dyes such as Acid Black 1 (AB 1). Since AB 1 contains negatively charged sulfonate (–SO_3^-) groups, favorable electrostatic attraction occurs when the catalyst surface is positively charged (pH < pHpzc). However, strongly acidic conditions may lead to excess protonation and reduced ROS transfer efficiency. On the other hand, at alkaline pH values (pH > pHpzc), electrostatic repulsion between the negatively charged catalyst surface and dye molecules hinders adsorption, thereby lowering degradation efficiency.

The optimal degradation performance observed at near-neutral pH (≈7.0) aligns well with the determined pHpzc of 6.88. Under this condition, the Tb–U–TiO_2 surface maintains a balanced charge environment that enhances dye adsorption while ensuring efficient reactive oxygen species (ROS) generation and transfer, ultimately maximizing photocatalytic activity. Thus, the determination of the pHpzc provides mechanistic insight into the interaction between Tb–U–TiO_2 and anionic dyes, demonstrating that fine-tuning the solution pH relative to the catalyst's surface charge characteristics is critical for optimizing photocatalytic water treatment processes.

Upon establishing pH 7 as the ideal condition for photocatalytic performance, subsequent experiments were carried out to examine how varying amounts of Tb-doped U-TiO_2 catalyst influence the breakdown efficiency. A series of catalyst doses (10–50 mg) was assessed under the

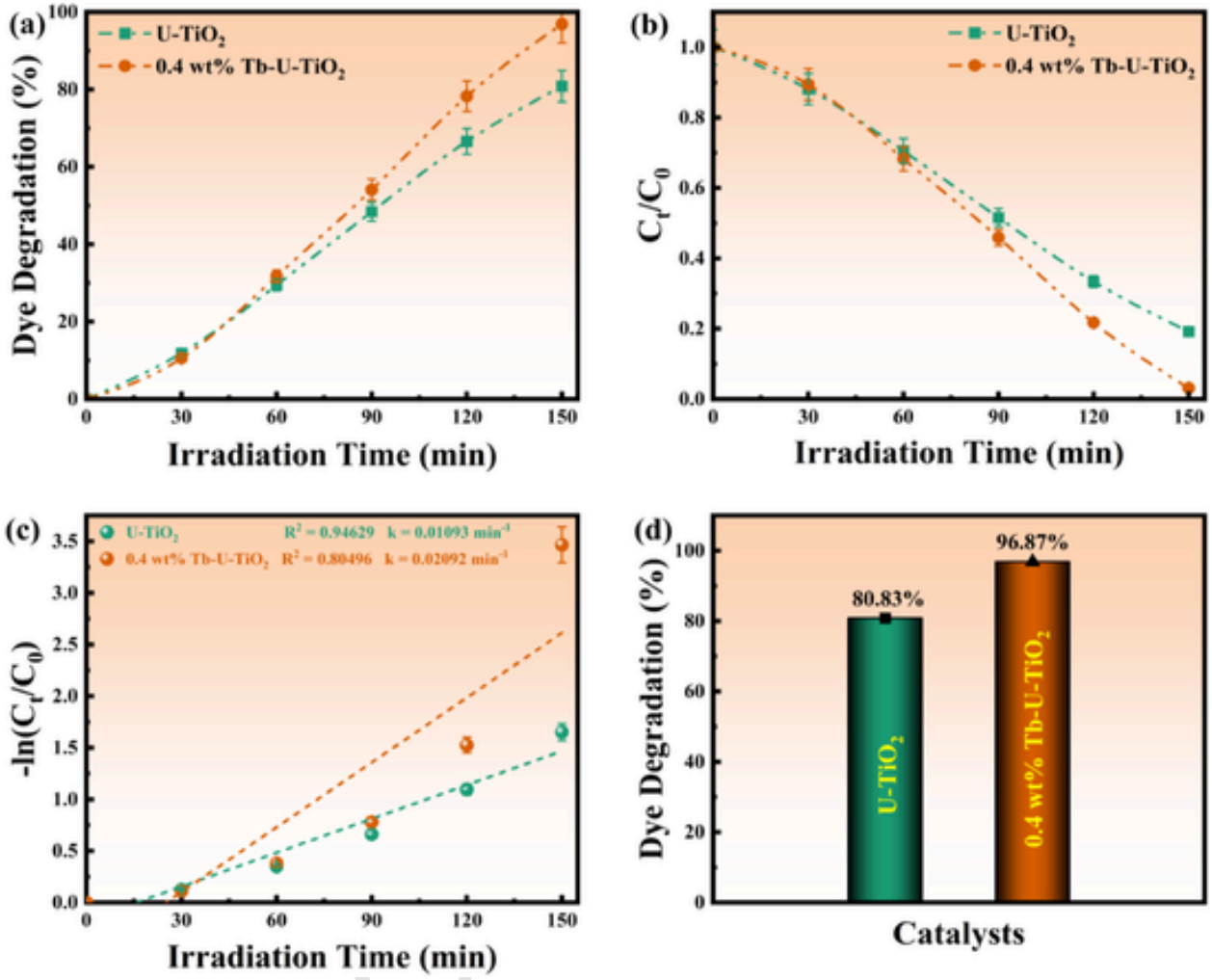

Fig. 9. (a) Photocatalytic degradation of Reactive Red 120 (RR 120) dye under natural sunlight using pristine U-TiO_2 and 0.4 wt % Tb-doped U-TiO_2 catalysts; (b) normalized concentration curves (C_t/C_0) tracked over irradiation time; (c) linearized pseudo-first-order kinetic plots illustrating degradation rates; and (d) comparative analysis of photocatalytic efficiencies for all samples after 150 min of sunlight exposure [Experimental conditions: catalyst dosage = 20 mg, dye concentration = 50 ppm, and pH = 7].

neutral pH conditions established. All samples were exposed to irradiation for 40 min, allowing for a direct comparison of photocatalytic performance across different catalyst loadings. Subsequent studies on the influence of catalyst dosage (Fig. 10b) revealed that increasing the amount of Tb-doped U-TiO_2 up to a certain point significantly enhanced dye degradation. At the lowest dosage of 10 mg, the degradation efficiency was 31.55 %, which increased substantially to 66.24 % with 20 mg of catalyst. Notably, near-complete degradation (≈100 %) was achieved at a dosage of 40 mg, with marginal differences observed for higher dosages of 30 mg (98.51 %) and 50 mg (97.82 %). The plateauing of efficiency at higher loadings suggests a saturation effect; once the dye molecules are fully adsorbed and degraded, adding more catalyst does not proportionally increase activity. In fact, excess catalyst may cause light scattering or shielding, thereby reducing the number of effective photons reaching the catalyst surface. In summary, the study clearly identifies pH 7 and a catalyst dosage of 40 mg as the most favourable conditions for efficient and economical photocatalytic elimination of AB 1 dye using Tb-doped U-TiO_2. These findings emphasize the need for careful tuning of reaction parameters to optimize photocatalyst performance, contributing significantly to the design of advanced water purification systems.

4.4. Catalyst stability and reactive species identification

A durability assessment was conducted to examine the sustained performance and structural stability of the optimized 0.4 wt % Tb-doped U-TiO_2 photocatalyst, targeting its viability for scalable environmental remediation efforts. This assessment served to verify not only the sustained photocatalytic performance across multiple usage cycles but also the material's resilience, an essential factor for real-world deployment in water purification systems. The catalyst underwent four successive degradation cycles, with its performance carefully monitored after each run. Impressively, the photocatalytic activity remained high, showing degradation efficiencies of approximately 100 %, 98.2 %, 96.5 %, and 94.2 % for the first through fourth cycles, respectively (refer to Fig. 10c). These results indicate only a slight decrease in efficiency, demonstrating the catalyst's excellent stability and endurance through repeated use. Such consistent results make this material a promising candidate for commercial applications, supporting both cost-effectiveness and environmental sustainability through reduced material loss and extended operational life.

After each cycle, the photocatalyst was recovered by filtration and then regenerated through a straightforward thermal treatment process. The harvested material was oven-dried at 100 °C for 1 h to remove any

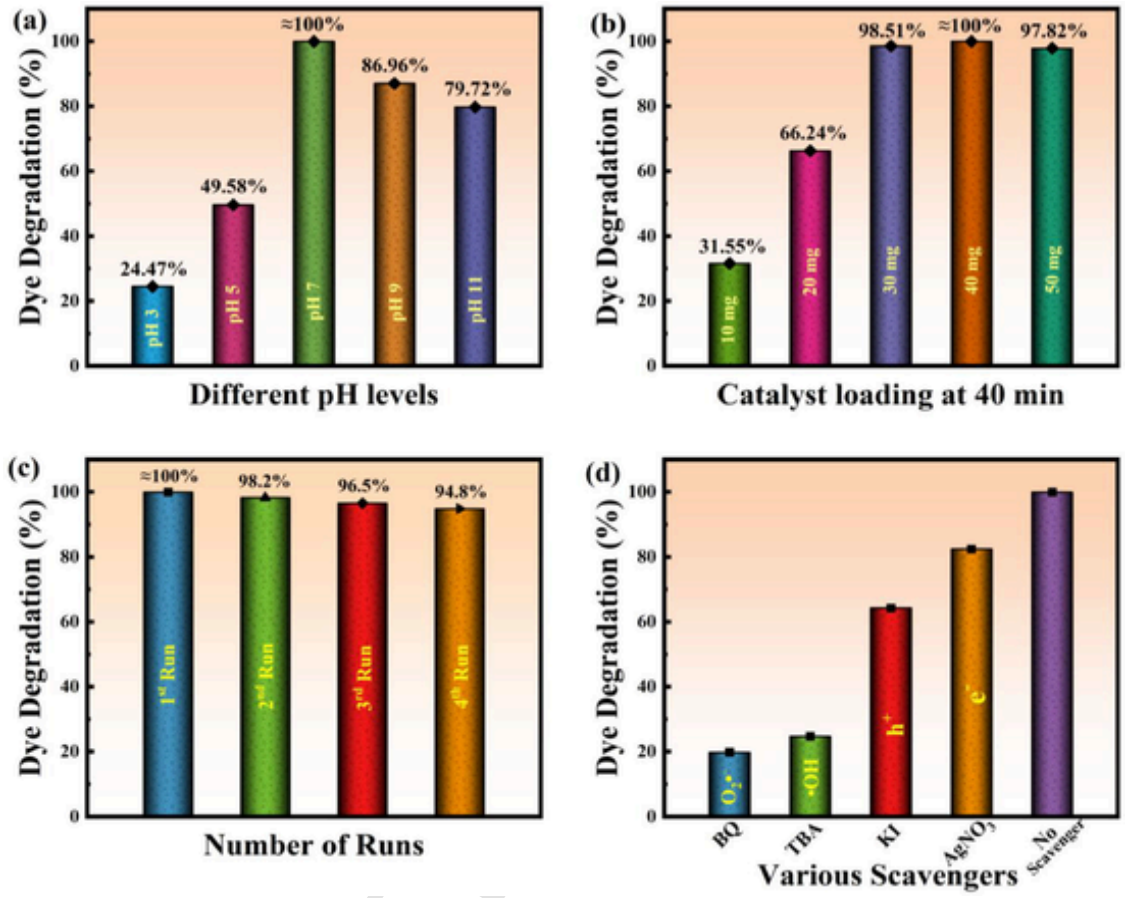

Fig. 10. (a) Influence of starting pH on the photocatalytic degradation efficiency of AB 1 dye with 20 mg of 0.4 wt % Tb-doped U-TiO_2 under UV-C irradiation for 60 min; (b) Effect of varying catalyst dosages (10–50 mg) on AB 1 dye degradation at 40 min, conducted under optimized conditions (pH 7) with 0.4 wt % Tb-doped U-TiO_2; (c) Photocatalyst reusability performance over four consecutive cycles, and (d) Influence of various scavengers on the breakdown efficiency of Acid Black 1 (AB 1) at pH 7 with 40 mg of 0.4 wt % Tb-doped U-TiO_2 under UV-C light exposure for 40 min.

residual moisture and surface-bound impurities. This mild regeneration step proved effective in restoring the photocatalyst without diminishing its activity, underscoring the material's practicality for continuous use in industrial water treatment operations.

Fig. 10d illustrates how different scavengers influence the photocatalytic degradation efficiency of the dye using 0.4 wt % Tb-doped U-TiO_2 under controlled conditions. These scavengers serve as essential probes to pinpoint the primary reactive species: such as superoxide radicals ($O_2^{\bullet-}$), hydroxyl radicals ($^{\bullet}OH$), photogenerated holes (h^+), and electrons (e^-), that drive the degradation process. By selectively quenching these active species, their individual contributions to the overall photocatalytic mechanism can be more precisely elucidated. When benzoquinone (BQ), a known quencher of superoxide radicals, was introduced, a dramatic drop in degradation efficiency to about 20 % was observed. This significant decline indicates that $O_2^{\bullet-}$ species are the dominant contributors to the photocatalytic activity. Likewise, the introduction of tert-butyl alcohol (TBA), a potent hydroxyl radical scavenger, caused the degradation efficiency to drop to approximately 30 %. While this confirms the participation of $^{\bullet}OH$ radicals, their role appears to be secondary to that of $O_2^{\bullet-}$. In experiments involving potassium iodide (KI), which targets photogenerated holes, the efficiency decreased to nearly 60 %, suggesting that holes also aid the degradation process, albeit to a lesser extent. The application of silver nitrate ($AgNO_3$), a scavenger of free electrons, resulted in a milder reduction in efficiency to about 80 %. This outcome implies that electrons do contribute to the photocatalytic reaction, but their impact is comparatively limited. Under scavenger-free conditions, the catalyst exhibited near-complete dye removal, close to 100 %, serving as the control benchmark and demonstrating the full potential of the Tb-doped U-TiO_2 system. From the comparative analysis of the scavenger data, the descending order of reactive species influence in the degradation process is established as: Superoxide radicals ($O_2^{\bullet-}$) dominate, followed by hydroxyl radicals ($^{\bullet}OH$), then photogenerated holes (h^+), and lastly electrons (e^-). This hierarchy underscores the pivotal role of superoxide radicals in enhancing the breakdown, guiding future optimization strategies for enhanced photocatalytic performance.

4.5. Degradation pathway and mechanism

4.5.1. AB 1 degradation proposed pathway based on GC–MS analysis

The photodegradation of Acid Black 1 (AB 1) dye under UV-C light in the presence of terbium-doped urea-derived TiO_2 (Tb-U-TiO_2) was comprehensively analyzed using gas chromatography–mass spectrometry (GC–MS). As summarized in **Table S6**, the GCMS– data revealed the presence of several degradation intermediates, identified based on their distinct molecular weights and fragmentation profiles. These observations facilitated the proposal of a detailed degradation mechanism, as illustrated in Fig. 11. During the photodegradation process, it is not uncommon for transient intermediates to exhibit greater toxicity than the parent dye molecule. In this context, five major degradation intermediate products (**DIP 1** to **DIP 5**) were detected. Among them, **DIP 1** identified as (*3E,6E*)-3-(2-(4-nitrophenyl)diazenyl)-6-(2-phenyldiazenyl)-4-

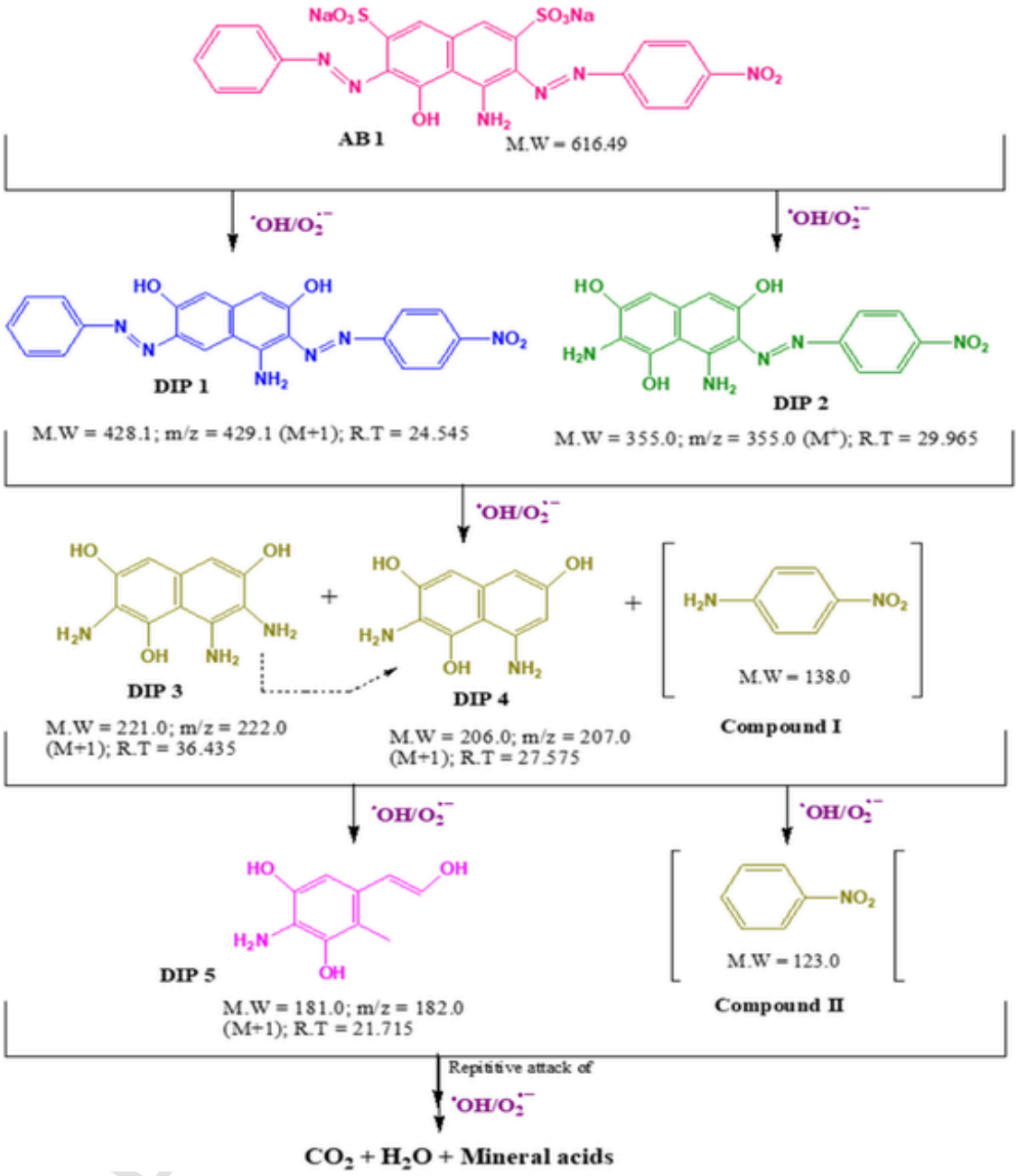

Fig. 11. Photocatalytic degradation pathway of AB 1 dye under UV-C light with Tb doped U-TiO_2.

aminonaphthalene-2,7-diol and **DIP 2** (E)-7-(2-(4-nitrophenyl) diazenyl)-2,8-diaminonaphthalene-1,3,6-triol were observed at retention times of 24.545 and 29.965 min, respectively. These intermediates likely originated from initial desulfonation and partial cleavage of the azo linkages within the AB 1 structure.

Subsequent transformations involved successive cleavage of remaining azo bonds and partial deamination reactions, leading to the formation of simpler aromatic amines such as **DIP 3** (2,7,8-triaminonaphthalene-1,3,6-triol) and **DIP 4** (2,8-diaminonaphthalene-1,3,6-triol). Notably, **DIP 4** could also be derived from **DIP 3** via further deamination. Another key fragment, identified as 4-nitrobenzenamine (denoted as Compound **I**), was generated during these transformations. Further degradation of **DIP 3** and **DIP 4** resulted in the cleavage of the naphthalene ring, yielding **DIP 5** (2-amino-5-((E)-2-hydroxyvinyl)-4-methylbenzene-1,3-diol) detected at a retention time of 21.715 min. Compound **I** underwent additional deamination to form compound **II**. Ultimately, both compound **II** and **DIP 5** were mineralized into harmless end products, including water (H_2O), carbon dioxide (CO_2), and mineral acids. This comprehensive degradation pathway underscores the capability of Tb doped U-TiO_2 photocatalyst to systematically dismantle the complex molecular structure of AB 1 into environmentally benign species. The stepwise breakdown not only ensures effective decolorization but also minimizes the risk posed by toxic intermediates, confirming the photocatalyst's potential in advanced wastewater treatment applications.

4.5.2. Mechanism of AB 1 degradation by Tb doped TiO_2

When exposed to UV-C or solar light, the Tb-doped urea-modified TiO_2 (Tb-U-TiO_2) photocatalyst harnesses the energy of incoming photons to excite electrons from the valence band (VB) to the conduction

band (CB), thereby generating electron–hole pairs, as illustrated in **Scheme S1** (see Supporting information). In conventional TiO_2, the rapid recombination of these charge carriers tends to hinder the efficiency of photocatalytic reactions. However, the strategic introduction of terbium ions into the TiO_2 lattice mitigates this drawback by creating oxygen vacancy sites and localized defect states that serve as efficient traps for charge carriers. These defect-induced trapping centers effectively capture photogenerated electrons, thereby suppressing their recombination with holes and extending their availability for participating in surface redox reactions. In addition, terbium incorporation subtly alters the band structure of TiO_2, potentially narrowing the bandgap or introducing intermediate states, which enhance the material's ability to utilize a broader spectrum of light, including portions of the visible region, making it more effective under solar irradiation.

Oxygen vacancies introduced by Tb doping play a pivotal role not only in separating charges but also in initiating the formation of highly reactive oxygen species (ROS) such as superoxide radicals ($O_2^{\bullet-}$) and hydroxyl radicals ($^{\bullet}OH$). These ROS act as key oxidative agents responsible for breaking down dye molecules and other organic contaminants. Furthermore, Tb doping improves the surface affinity of the catalyst towards polar molecules, thereby increasing its hydrophilicity. This modification enhances the adsorption of dye molecules on the photocatalyst surface, facilitating more effective interaction between the catalyst and pollutants. Altogether, the collective contributions of improved light harvesting, suppressed charge recombination, enhanced ROS production, and improved surface properties lead to a significant boost in the photocatalytic performance of Tb-U-TiO_2. These enhancements enable efficient degradation of dyes under both UV-C and natural sunlight, making this material a promising candidate for environmental remediation applications.

4.6. Antibacterial activity and literature comparison

The antibacterial performance of 0.4 wt % Tb-doped U-TiO_2 was evaluated against both Gram ± bacterial strains, including *Staphylococcus aureus, Pseudomonas aeruginosa, Bacillus subtilis*, and *Escherichia coli* (Fig. 12). The efficacy was assessed by measuring the inhibition zones at varying concentrations (60, 80, and 100 μg/mL) were measured and compared against the bare U-TiO_2, 0.4 wt % Tb-U- TiO_2 and a standard antibiotic, Amoxicillin (Fig. 12a & b). The Tb-doped photocatalyst displayed a substantial improvement in antibacterial activity compared to the undoped counterpart. For *S. aureus*, a Gram-positive pathogen, the zone of inhibition progressively increased with concentration, measuring 4 mm, 6 mm, and 8 mm at 60, 80, and 100 μg/mL, respectively. This enhancement indicates an improved bactericidal effect likely due to augmented generation of reactive oxygen species under light irradiation facilitated by terbium incorporation. Similarly, the growth suppression zones for *P. aeruginosa*, a Gram-negative bacterium known for its resistance to antibiotics, showed significant improvement with Tb doping. The inhibition reached up to 9 mm at 100 μg/mL, which was markedly higher than the 3 mm observed for the bare U-TiO_2 at the same concentration. This suggests that the Tb dopant not only improves photocatalytic activity but also contributes to greater disruption of bacterial cell membranes. *B. subtilis* showed moderate sensitivity to the Tb-modified photocatalyst, with inhibition zones measuring 3 mm, 4 mm, and 5 mm at the respective concentrations tested. Although less than those for *S. aureus* and *E. coli*, these values still represent a noticeable enhancement compared to the undoped sample, which showed minimal to no activity. *E. coli*, another Gram-negative strain, exhibited one of the most notable responses to Tb-doping, with the inhibition zone reaching 10 mm at the highest concentration, a substantial increase

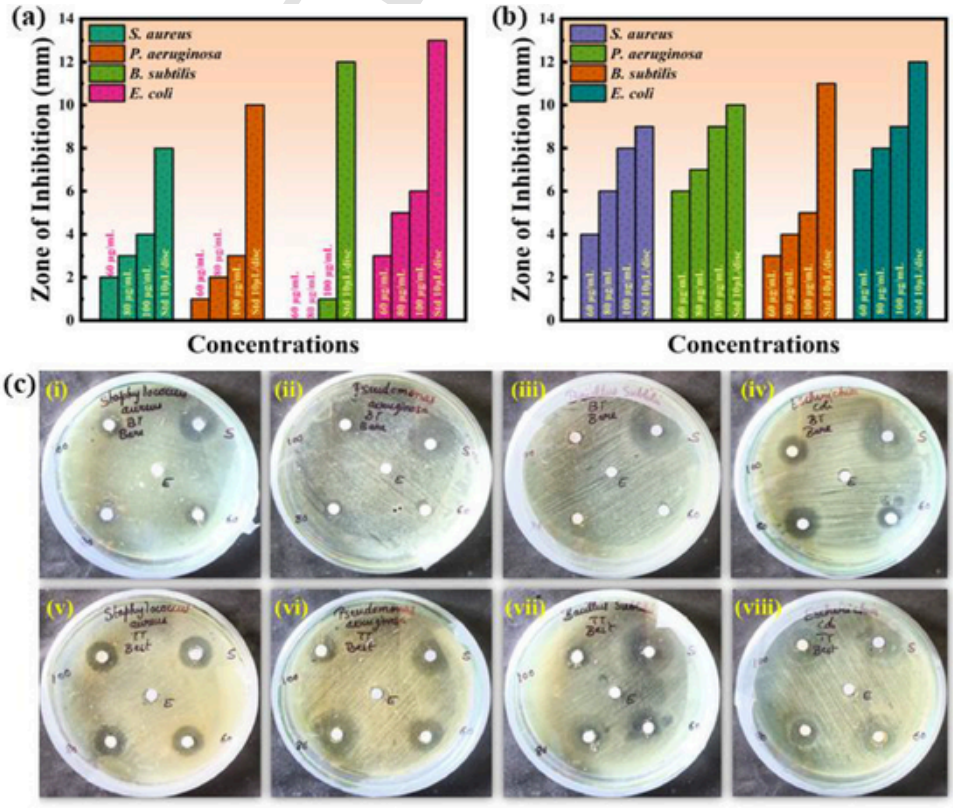

Fig. 12. Bar chart illustrating the antibacterial activity comparison between (a) Bare U-TiO_2 and (b) 0.4 wt % Tb-doped U-TiO_2 photocatalysts. (c) Antibacterial response was assessed against four bacterial strains: (i) *Staphylococcus aureus*, (ii) *Pseudomonas aeruginosa*, (iii) *Bacillus subtilis*, and (iv) *Escherichia coli* using Bare U-TiO_2, and (v) *Staphylococcus aureus*, (vi) *Pseudomonas aeruginosa*, (vii) *Bacillus subtilis*, and (viii) *Escherichia coli* using 0.4 wt % Tb-doped U-TiO_2.

CORRECTED PROOF

from the 6 mm noted for undoped U-TiO_2. The high sensitivity of *E. coli* to the Tb-doped photocatalyst underlines its potential application against waterborne and antibiotic-resistant pathogens. The control experiments using aqueous solution showed no inhibition, confirming that the noted antibacterial responses were due to the photocatalyst. (Fig. 12c) Conversely, the standard antibiotic, Amoxicillin, displayed strong inhibition across all strains, serving as a benchmark for comparison. The observed improvements in antibacterial activity upon terbium doping are attributed to enhanced charge separation and increased ROS formation under irradiation, which are critical for microbial inactivation. These findings suggest that Tb-doped U-TiO_2 is a promising material for developing antimicrobial coatings or water purification systems, offering a sustainable and effective solution against a broad spectrum of bacterial contaminants.

The comparative analysis of various Tb-based photocatalysts highlights the superior performance of the synthesized 0.4 wt % Tb-U-TiO_2 composite for dye degradation under both UV-C and solar irradiation. Several reported studies have investigated the photocatalytic efficiency of Tb-doped materials under different conditions and with various pollutants, as shown in Table 1. For instance, Tb-doped ZnO exhibited 90 % degradation of Rhodamine B (5 ppm) in 150 min under a 100 W tungsten lamp at pH 12 using a 20 mg/100 mL dosage [58]. Tb–$BiFeO_3$/CNTs achieved 63.5 % degradation of Crystal Violet (7 ppm) in 140 min under a 250 W tungsten bulb [59]. Another study employed Tb-doped Mg–$CdAl_2O_4$ with MXene under solar light, reaching 86.2 % degradation of Rhodamine B (10 ppm) within 90 min [60]. Similarly, Tb-doped CuO demonstrated 94 % removal of Methylene Blue (3.2 mg/L) in 120 min under a 300 W halogen lamp [61], while Tb-doped SnO_2, under UV light (254 nm), achieved 85 % degradation of Methylene Blue (1×10^{-5} M) over 125 min [62]. A Tb-doped ZnO/RGO hybrid reached 96 % degradation of Rhodamine B (20 ppm) in 120 min using a 300 W xenon lamp at neutral pH [63]. Compared to these systems, the present study Tb-U-TiO_2 photocatalyst stands out due to its rapid and highly efficient degradation of dyes under both artificial and natural light. It attained almost total (≈100 %) breakdown of Acid Black 1 (20 ppm) within just 40 min under UV-C light (32 W, 254 nm) at pH 7, and 96.87 % removal of Reactive Red 120 (50 ppm) under solar light in 150 min at the same pH. The elevated photocatalytic response can be credited to the mutual enhancement provided by Tb and urea co-modification, which enhances light absorption, promotes effective charge carrier separation, and increases the induction of reactive oxygen species. This establishes Tb-U-TiO_2 as a highly efficient and environmentally sustainable photocatalyst for the treatment of dye-laden wastewater

Table 1
Comparative evaluation of photocatalytic efficiency of Tb-U-TiO_2 with reported Tb-based photocatalysts for dye degradation under light irradiation.

S. No	Catalysts	Light source	Pollutants/ Concentration	Catalyst dosage	Degradation (%)/ time (min) & pH	Ref
1	Tb-doped ZnO	100 W tungsten lamp	Rhodamine B/ 5 ppm	20 mg/ 100 mL	90/150 at pH 12	[58]
2	Tb-$BiFeO_3$/CNTs	250 W tungsten bulb	Crystal Violet/ 7 ppm	30 mg/ 60 mL	63.5/140 at pH -	[59]
3	Tb-doped Mg–$CdAl_2O_4$ with MXene	Solar light	Rhodamine B/ 10 ppm	20 mg/ 70 mL	86.2/90 at pH -	[60]
4	Tb doped CuO	300 W tungsten halogen amp	Methylene Blue/ 3.2 mg/L	75 mg / 400 mL	94/120 at pH -	[61]
5	Tb-doped SnO_2	UV lamp (254 nm)	Methylene Blue/ 1×10^{-5} M	- / 100 mL	85/125 at pH -	[62]
6	Tb-doped ZnO/RGO	300 W xenon lamp	Rhodamine B/ 20 ppm	30 mg/ 50 mL	96/120 at pH 7	[63]
7	0.4 wt % Tb-U-TiO_2	32 W-UV-C light, 254 nm, and solar	Acid Black 1/20 ppm Reactive Red 120/ 50 ppm	50 mg/ 100 mL 20 mg/ 100 mL	≈100/40 at pH 7 (UV) 96.87/150 at pH 7 (solar)	**[Present work]**

5. Conclusion

In this study, we have successfully engineered a multifunctional, urea-modified Tb-doped TiO_2 nanocomposite via a simple sol–gel approach, achieving remarkable efficiency in both azo dye degradation and antibacterial performance. The strategic integration of terbium doping and urea tailoring significantly enhanced photonic absorption in the UV region, accelerated charge carrier dynamics, and active surface interactions. This innovation translated into exceptional photocatalytic activity, with 0.4 wt % Tb-doped U-TiO_2 exhibiting superior performance compared to other Tb loadings (0.2 wt % and 0.8 wt %) and bare U-TiO_2. It achieved 86.01 % and 87.6 % degradation of Acid Black 1 with the 0.2 wt % and 0.8 wt % catalysts, respectively, while the 0.4 wt % sample achieved complete mineralization under UV-C light within 60 min. Additionally, it removed nearly 97 % of Reactive Red 120 under sunlight, significantly outperforming bare U-TiO_2, which showed only 80.83 % removal in 150 min. The optimal conditions were identified as pH 7 and 40 mg of catalyst loading under UV-C light, achieving complete degradation of AB 1 within 40 min. Trapping experiments revealed that superoxide radicals ($O_2^{\bullet-}$) were the dominant reactive species, followed by hydroxyl radicals ($^{\bullet}OH$), photogenerated holes (h^+), and electrons (e^-). Additionally, the catalyst exhibited robust antimicrobial efficacy against both Gram ± bacteria, addressing dual concerns of chemical pollutants and microbial pathogens in wastewater streams. With superior stability, reusability, and eco-compatibility, this nano photocatalyst stands as a next-generation platform for sustainable water purification. Its dual-action potential, solar-driven dye detoxification and microbial disinfection; makes it a smart, scalable solution for addressing critical environmental challenges. The findings not only deepen the scientific understanding of dopant-synergized photocatalysis but also pave the way for real-world deployment in industrial and municipal wastewater treatment frameworks.

Authors statement

Finally, authors of this work would like to note that this paper is an original work, not previously published, submitted or under consideration at any other journal. All authors agree to submit the article to ***Surfaces and Interfaces***.

Data availability statement

The data that support the findings of this study are available from the corresponding author upon reasonable request.

CRediT authorship contribution statement

Sharon Leela N: Writing – original draft, Methodology, Investigation, Data curation, Conceptualization. **Kannan S:** Writing – review & editing, Supervision, Conceptualization. **T. Abisheik:** Writing – review & editing, Software, Data curation. **V. Pandiyan:** Writing – review & editing, Validation. **Abdullah K. Alanazi:** Software, Data curation. **A. Raja:** Visualization, Software. **Parvathalu Kalakonda:** Writing – review & editing, Validation. **Arun Thirumurugan:** Software, Data curation. **Gabriela Sandoval-Hevia:** Visualization, Soft-

CORRECTED PROOF

ware. **Krishnakumar Balu:** Writing – review & editing, Supervision, Conceptualization.

Declaration of competing interest

The authors declare that they have no known competing financial interests or personal relationships that could have appeared to influence the work reported in this paper.

Acknowledgments

We acknowledge the Nanotechnology Research Centre (NRC), SRM IST, for providing the research facilities.

Data availability

Data will be made available on request.

Supplementary materials

Supplementary material associated with this article can be found, in the online version, at doi:10.1016/j.surfin.2025.107909.

References

[1] A.P. Periyasamy, Recent advances in the remediation of textile-dye-containing wastewater: prioritizing human health and sustainable wastewater treatment, Sustainability. 16 (2) (2024) 495.
[2] A. Ajmal, I. Majeed, R.N. Malik, H. Idriss, M.A. Nadeem, Principles and mechanisms of photocatalytic dye degradation on TiO_2 based photocatalysts: a comparative overview, RSC. Adv. 4 (70) (2014) 37003–37026.
[3] A. Gürses, M. Açıkyıldız, K. Güneş, M.S. Gürses, A. Gürses, M. Açıkyıldız, K. Güneş, M.S. Gürses, Colorants in health and environmental aspects, Dyes. Pigm. (2016) 69–83.
[4] J. Sharma, S. Sharma, V. Soni, Classification and impact of synthetic textile dyes on Aquatic Flora: a review, Reg. Stud. Mar. Sci. 45 (2021) 101802.
[5] M.A.M. Salleh, D.K. Mahmoud, W.A.W.A. Karim, A. Idris, Cationic and anionic dye adsorption by agricultural solid wastes: a comprehensive review, Desalination. 280 (1–3) (2011) 1–13.
[6] A. Ketema, A. Worku, Review on intermolecular forces between dyes used for polyester dyeing and polyester fiber, J. Chem. 2020 (1) (2020) 6628404.
[7] A. Tkaczyk, K. Mitrowska, A. Posyniak, Synthetic organic dyes as contaminants of the aquatic environment and their implications for ecosystems: a review, Sci. Total. Environ. 717 (2020) 137222.
[8] D. Rawat, V. Mishra, R.S. Sharma, Detoxification of azo dyes in the context of environmental processes, Chemosphere 155 (2016) 591–605.
[9] F. Uddin, Environmental hazard in textile dyeing wastewater from local textile industry, Cellulose 28 (17) (2021) 10715–10739.
[10] B. Lellis, C.Z. Fávaro-Polonio, J.A. Pamphile, J.C. Polonio, Effects of textile dyes on health and the environment and bioremediation potential of living organisms, Biotechnol. Res. Innov. 3 (2) (2019) 275–290.
[11] J. Sharma, S. Sharma, V. Soni, Toxicity of malachite green on plants and its phytoremediation: a review, Reg. Stud. Mar. Sci. 62 (2023) 102911.
[12] R. Kuhn, I.M. Bryant, R. Jensch, J. Böllmann, Applications of environmental nanotechnologies in remediation, wastewater treatment, drinking water treatment, and agriculture, Applied Nano 3 (1) (2022) 54–90.
[13] K. Singh, S. Arora, Removal of synthetic textile dyes from wastewaters: a critical review on present treatment technologies, Crit. Rev. Environ. Sci. Technol. 41 (9) (2011) 807–878.
[14] A. Haleem, A. Shafiq, S.Q. Chen, M. Nazar, A comprehensive review on adsorption, photocatalytic and chemical degradation of dyes and nitro-compounds over different kinds of porous and composite materials, Molecules. 28 (3) (2023) 1081.
[15] D. Lan, H. Zhu, J. Zhang, S. Li, Q. Chen, C. Wang, T. Wu, M. Xu, Adsorptive removal of organic dyes via porous materials for wastewater treatment in recent decades: a review on species, mechanisms and perspectives, Chemosphere 293 (2022) 133464.
[16] A.B. Ponnusami, S. Sinha, H. Ashokan, M.V. Paul, S.P. Hariharan, J. Arun, K.P. Gopinath, Q.H. Le, A. Pugazhendhi, Advanced oxidation process (AOP) combined biological process for wastewater treatment: a review on advancements, feasibility and practicability of combined techniques, Environ. Res. 237 (2023) 116944.
[17] M.L. Marin, L. Santos-Juanes, A. Arques, A.M. Amat, M.A. Miranda, Organic photocatalysts for the oxidation of pollutants and model compounds, Chem. Rev. 112 (3) (2012) 1710–1750.
[18] F. Mohamadpour, A.M. Amani, Photocatalytic systems: reactions, mechanism, and applications, RSC. Adv. 14 (29) (2024) 20609–20645.
[19] R. Ghamarpoor, A. Fallah, M. Jamshidi, A review of synthesis methods, modifications, and mechanisms of ZnO/TiO_2-based photocatalysts for photodegradation of contaminants, ACS. Omega 9 (24) (2024) 25457–25492.
[20] X. Liu, Y. Yan, Z. Da, W. Shi, C. Ma, P. Lv, Y. Tang, G. Yao, Y. Wu, P. Huo, Y. Yan, Significantly enhanced photocatalytic performance of CdS coupled WO_3 nanosheets and the mechanism study, Chem. Eng. J. 241 (2014) 243–250.
[21] A. Pattnaik, J.N. Sahu, A.K. Poonia, P. Ghosh, Current perspective of nano-engineered metal oxide based photocatalysts in advanced oxidation processes for degradation of organic pollutants in wastewater, Chem. Eng. Res. Des. 190 (2023) 667–686.
[22] Z. Wang, Y. Liu, B. Huang, Y. Dai, Z. Lou, G. Wang, X. Zhang, X. Qin, Progress on extending the light absorption spectra of photocatalysts, Phys. Chem. Chem. Phys. 16 (7) (2014) 2758–2774.
[23] P. Zhang, T. Wang, X. Chang, J. Gong, Effective charge carrier utilization in photocatalytic conversions, Acc. Chem. Res. 49 (5) (2016) 911–921.
[24] M. Pelaez, N.T. Nolan, S.C. Pillai, M.K. Seery, P. Falaras, A.G. Kontos, P.S. Dunlop, J.W. Hamilton, J.A. Byrne, K. O'shea, M.H. Entezari, A review on the visible light active titanium dioxide photocatalysts for environmental applications, Appl. Catal., B 125 (2012) 331–349.
[25] D. Chen, Y. Cheng, N. Zhou, P. Chen, Y. Wang, K. Li, S. Huo, P. Cheng, P. Peng, R. Zhang, L. Wang, Photocatalytic degradation of organic pollutants using TiO_2-based photocatalysts: a review, J. Clean. Prod. 268 (2020) 121725.
[26] H. Dong, G. Zeng, L. Tang, C. Fan, C. Zhang, X. He, Y. He, An overview on limitations of TiO2-based particles for photocatalytic degradation of organic pollutants and the corresponding countermeasures, Water. Res. 79 (2015) 128–146.
[27] C.B. Anucha, I. Altin, E. Bacaksiz, V.N. Stathopoulos, Titanium dioxide (TiO_2)-based photocatalyst materials activity enhancement for contaminants of emerging concern (CECs) degradation: in the light of modification strategies, Chem. Eng. J. Adv. 10 (2022) 100262.
[28] D. Palariya, S. Mehtab, M. Aziz, M.G.H. Zaidi, Exploring rare earth element doped nanocomposites as promising photocatalysts for dyes degradation in water, Water. Air. Soil. Pollut. 235 (5) (2024) 286.
[29] E. Cerrato, E. Gaggero, P. Calza, M.C. Paganini, The role of Cerium, Europium and Erbium doped TiO_2 photocatalysts in water treatment: a mini-review, Chem. Eng. J. Adv. 10 (2022) 100268.
[30] C.S. You, S.C. Jung, Photo-catalytic destruction of tetracycline antibiotics using terbium and manganese co-precipitated TiO_2 photocatalyst, J. Environ. Chem. Eng. 12 (1) (2024) 111666.
[31] M.T. Colomer, E. Rodríguez, M. Morán-Pedroso, F. Vattier, A. de Andrés, Impact of Tb^{4+} and morphology on the thermal evolution of Tb-doped TiO_2 nanostructured hollow spheres and nanoparticles, J. Alloys. Compd. 853 (2021) 156973.
[32] S. tul Shafa, B. Basha, Z.A. Alrowaili, M. Imran, M. Sohail, M.S. Al-Buriahi, M. Shahid, M.F. Warsi, Synthesis and characterization of Cu and Tb substituted $NiFe_2O_4$@ MXene nanocomposite as a new photocatalyst for removal of organic dyes and drugs from industrial wastewater, Results. Phys. 63 (2024) 107844.
[33] L. Lianmawii, N.M. Singh, Effect of additives on the photocatalytic degradation of malachite green using NiS: tb^{3+} nanoparticle and their photoluminescence properties, J. Mol. Struct. 1320 (2025) 139748.
[34] N.S. Arul, D. Mangalaraj, T.W. Kim, Photocatalytic degradation mechanisms of CeO_2/Tb_2O_3 nanotubes, Appl. Surf. Sci. 349 (2015) 459–464.
[35] N. AlMasoud, A. Irshad, U. Rafiq, T.S. Alomar, A.A. Al-wallan, M.F. Warsi, Z.M. El-Bahy, Sol-gel synthesis of Tb-doped lithium-nickel ferrite anchored onto g-C_3N_4 sheets for efficient photocatalytic degradation of organic dyes, Ceram. Int. 50 (22) (2024) 46892–46903.
[36] L. Mao, Y. Wang, Y. Zhong, J. Ning, Y. Hu, Microwave-assisted deposition of metal sulfide/oxide nanocrystals onto a 3D hierarchical flower-like TiO_2 nanostructure with improved photocatalytic activity, J. Mater. Chem. A 1 (28) (2013) 8101–8104.
[37] P.S. Shen, Y.C. Tai, P. Chen, Y.C. Wu, Clean and time-effective synthesis of anatase TiO_2 nanocrystalline by microwave-assisted solvothermal method for dye-sensitized solar cells, J. Power. Sources. 247 (2014) 444–451.
[38] S. Mathew, A.K. Prasad, T. Benoy, P.P. Rakesh, M. Hari, T.M. Libish, P. Radhakrishnan, V.P.N. Nampoori, C.P.G. Vallabhan, UV–visible photoluminescence of TiO_2 nanoparticle prepared by hydrothermal method, J. Fluor. 22 (2012) 1563–1569.
[39] H. Chen, D. Chen, L. Bai, K. Shu, Hydrothermal synthesis and electrochemical properties of TiO_2 nanotubes as an anode material for lithium ion batteries, Int. J. Electrochem. Sci. 13 (2018) 2118–2125.
[40] K. Shi, Z. Wang, J. Luo, et al., Construction of novel NH_2-Al-SBA-15 based mesoporous molecular sieve and application in the adsorption of methylene blue, J. Porous Mater. 31 (2024) 2017–2029.
[41] Y.F. Chen, C.Y. Lee, M.Y. Yeng, H.T. Chiu, The effect of calcination temperature on the crystallinity of TiO_2 nanopowders, J. Cryst. Growth 247 (2003) 363–370.
[42] H. Martinez, A.A. Amaya, E.A. Paez-Mozo, F. Martinez, S. Valange, Photo-assisted oatom transfer to monoterpenes with molecular oxygen and a dioxoMo (VI) complex immobilized on TiO_2 nanotubes, Catal. Today 375 (2021) 441–457.
[43] K. Balu, T. Abisheik, W. Ali, M.E. Khan, S.K. Ali, W. Ahmad, A.H. Bashri, V. Pandiyan, Y.H. Ahn, Reduced graphene oxide loaded sulfated titania mediated photocatalytic degradation of Reactive Red 120 dye under UV-A and solar light, Spectrochim. Acta a Mol. Biomol. Spectrosc. 338 (2025) 126184.
[44] V. Mariyappillai, C. Shiyamala, T. Abisheik, M. Tiffany, V. Pandiyan, A. Senthilraja, M. Afzal, P. Barmavatu, K. Shanmugaraj, K. Balu, Zr-modified ZnO nanoparticles: optimized photocatalytic degradation and antibacterial efficiency for pollution control, Ceram. Int. (2025).
[45] S. Landi Jr, I.R. Segundo, C. Afonso, O. Lima Jr, M.F. Costa, E. Freitas, J. Carneiro, Evaluation of band gap energy of TiO_2 precipitated from titanium

CORRECTED PROOF

sulphate, Physica B: Condens. Matter 639 (2022) 414008.
[46] Y. Guo, X. Fu, Y. Xie, L. Zhu, R. Liu, L. Liu, Synthesis of Ag/ZnO nanocomposites with enhanced visible photocatalytic performance, Opt. Mater. 133 (2022) 112980.
[47] B. Choudhury, A. Choudhury, Oxygen defect dependent variation of band gap, Urbach energy and luminescence property of anatase, anatase-rutile mixed phase and of rutile phases of TiO_2 nanoparticles, Phys. E 56 (2014) 364–371.
[48] Y. Lei, L.D. Zhang, G.W. Meng, G.H. Li, X.Y. Zhang, C.H. Liang, W. Chen, S.X. Wang, Preparation and photoluminescence of highly ordered TiO_2 nanowire arrays, Appl. Phys. Lett. 78 (2001) 1125–1127.
[49] V.R. Akshay, B. Arun, Guruprasad Mandal, M. Vasundhara, Visible range optical absorption, Urbach energy estimation and paramagnetic response in Cr-doped TiO_2 nanocrystals derived by a sol-gel method, Phys. Chem. Chem. Phys. 21 (2019) 12991.
[50] J.D. Bryan, S.A. Santangelo, S.C. Keveren, D.R. Gamelin, Activation of high-TC ferromagnetism in Co^{2+}: tiO_2 and Cr^{3+}: tiO_2 nanorods and nanocrystals by grain boundary defects, J. Am. Chem. Soc. 127 (2005) 15568–15574.
[51] W. Moloto, P.J. Mafa, P. Mbule, E. Nxumalo, B. Ntsendwana, Photoinduced electrochemical effect of porous BiPOM on TiO_2 photoanode performance for dye-sensitized solar cells application, Mater. Today Commun. 30 (2022) 103001.
[52] R. Ratshiedana, P.J. Mafa, O.J. Fakayode, A.K. Mishra, A.T. Kuvarega, Ag doped TiO_2 anchored on metal free g-C_3N_4 for enhanced solar light activated photodegradation of a dye, Opt. Mater. 157 (2024) 116125.
[53] P.J. Mafa, M.E. Malefane, A.O. Oladipo, S.L. Lebelo, D. Liu, J. Gui, B.B. Mamba, A.T. Kuvarega, Epitaxial construction of $BiPO_4$@ Bi (OH) 3vac S-scheme heterojunction with firm interfacial contact for bolstered photocatalytic performance, J. Environ. Chem. Eng. (2025) 117821.
[54] N. Sharon Leela, S. Kannan, T. Abisheik, M. Tiffany, V. Pandiyan, G. Periyasami, P. Barmavatu, K. Shanmugaraj, K. Balu, Enhanced photocatalytic activity of azo dyes degradation by urea assisted Mo-doped TiO_2 under UV-A light and sunlight irradiation, J. Alloys. Compd. 1020 (2025) 179389.
[55] H.A. El-Sabban, A.H. Mady, M.A. Diab, W.A. Zoubi, J.H. Kang, Y.G. Ko, Novel environmentally-friendly 0D/3D TiO_2@$FeMoO_4$ binary composite with boosted photocatalytic performance: structural analysis and Z-scheme interpretations, J. Alloy. Compd. 1010 (2025) 177265.
[56] S.K. Nzaba, O.K. Mmelesi, M.E. Malefane, P.J. Mafa, B.B. Mamba, A.T. Kuvarega, Comparative study of visible-light active BiOI and N, Pd-TiO_2 photocatalysts: catalytic ozonation for dye degradation, Colloids Surf., A 684 (2024) 133167.
[57] P.J. Mafa, M.E. Malefane, F. Opoku, J. Gui, D. Liu, B.B. Mamba, A.T. Kuvarega, Heightened photocatalytic performance of $ZnMoO_4$ by incorporation of cobalt heteroatom to enhance oxygen defects for boosted pharmaceutical degradation, J. Water. Process. Eng. 68 (2024) 106405.
[58] S. Hareeshanaik, M.C. Prabhakara, H.B. Naik, G. Vishnu, Photocatalytic, antibacterial and optoelectronic applications of terbium doped zinc oxide nanoparticles prepared via chemical co-precipitation method, Ceram. Int. 50 (20) (2024) 39748–39762.
[59] M.F. Abou Taleb, M. Afaq, H.A. Albalwi, F.I. Abou El Fadl, A. Irshad, M.M. Ibrahim, Tb-doped $BiFeO_3$ nanostructure and its composite with CNTs to improve the light-harvesting properties, Mater. Sci. Eng., B 299 (2024) 116916.
[60] S. Fatima, M. Anwar, A.S. Almalki, A. Alhadhrami, M.F. Warsi, Z.M. El-Bahy, Fabrication of rare earth (Tb^{+3}) and alkaline earth metal (Mg^{+2}) Co-doped $CdAl_2O_4$@xene composite: a unique approach to tune bandgap energy through quantum confinement effect for photocatalytic applications, Ceram. Int. 50 (17) (2024) 29201–29212.
[61] L.V. Devi, S. Sellaiyan, T. Selvalakshmi, H.J. Zhang, A. Uedono, K. Sivaji, S. Sankar, Synthesis, defect characterization and photocatalytic degradation efficiency of Tb doped CuO nanoparticles, Adv. Powder. Technol. 28 (11) (2017) 3026–3038.
[62] I.L.P. Raj, M.S. Revathy, A.J. Christy, N. Chidhambaram, V. Ganesh, S. AlFaify, Study on the synergistic effect of terbium-doped SnO_2 thin film photocatalysts for dye degradation, J. NanoPart Res. 22 (2020) 1–14.
[63] X. Dong, X. Yu, X. Zhang, Z. Zhang, X. He, R. Wei, Y. Bai, J. Fan, Synthesis of Tb-doped ZnO/RGO nanocomposites and its enhanced photocatalytic activity under visible light irradiation, Diam. Relat. Mater. 133 (2023) 109765.

CORRECTED PROOF